Received: 9 August 2021 | Revised: 18 November 2021 | Accepted: 24 January 2022

DOI: 10.1111/jmg.12656

ORIGINAL ARTICLE

Journal of METAMORPHIC GEOLOGY WILEY

Thorium zoning in monazite: A case study from the Ivrea–Verbano zone, NW Italy

Megan A. Williams[1,2] | **David E. Kelsey**[1,3] | **Daniela Rubatto**[4]

[1]Department of Earth Sciences, University of Adelaide, Adelaide, South Australia, Australia

[2]Department for Energy and Mining, Geological Survey of South Australia, Adelaide, South Australia, Australia

[3]Geological Survey of Western Australia, East Perth, Western Australia, Australia

[4]Institute of Geological Sciences, University of Bern, Bern, Switzerland

Correspondence
Megan A. Williams, Department for Energy and Mining, Geological Survey of South Australia, Adelaide, South Australia, Australia.
Email: megan.williams5@sa.gov.au

Handling Editor: Prof. Simon Harley

Abstract

Metamorphism and partial melting of the lower crust is commonly assumed to cause depletion in heat producing elements (HPEs; K, U, Th). In the deep crust, volumetrically subordinate metasedimentary layers, which are source to crustal granites (sensu *lato*), host the majority of Th ± U, primarily within the REE + Th + U + Y phosphate mineral monazite. We examine the spatial and temporal distribution of Th within monazite grains in metasedimentary rocks from the lower crustal section of the Ivrea–Verbano Zone (Italy), using textural, compositional and geochronological data. We link this to outcrop and regional scale trends described by in-field gamma-ray spectrometry data (in-field GRS) for the purpose of understanding how Th distribution is controlled by progressive metamorphism and partial melting. In-field GRS data shows that the whole rock budget of Th does not change between granulite facies rocks and their unmelted equivalents but is significantly lower in rocks that have undergone more significant melt loss at ultra-high temperature (UHT) conditions. Concurrently, the bulk Th budget of monazite increases with metamorphic grade to granulite facies conditions and is greatly reduced in UHT samples. Monazite geochronology returns dates mostly in the range 240–320 Ma with two main peaks at circa 290 and 270 Ma. Textural and chemical constraints indicate that these dates record the timing of pre-peak to peak metamorphic conditions. Amphibolite facies monazite compositional zones are absent from granulite facies monazite, in contrast to examples from lower-pressure terranes. This is consistent with the expanded stability of allanite relative to monazite with increasing pressure having an important role in determining the internal structure, composition and extent of inheritance of monazite in going from amphibolite facies to granulite facies rocks. We propose high-pressure granulites should preserve less monazite inherited from amphibolite facies conditions than low-pressure granulites. Monazite is preserved at all metamorphic grades and presents a mineralogical mechanism for retaining Th in residual deep crust during partial melting and after melt loss.

KEYWORDS
electron probe microanalysis, monazite chemistry, radiogenic heat production, U–Pb monazite geochronology

1 | INTRODUCTION

Monazite is a common accessory mineral in clastic metasediments across a wide range of pressure and temperature conditions and tectonic settings in the crust (e.g., Engi, 2017; Parrish, 1990). Its utility and significance far outweighs its low modal abundance: monazite is an important geochronometer for high temperature crustal processes and the major host of Th—a major heat producing element—in the crust. Despite extensive study of the chemical behaviour of the rare earth elements (REEs) and Y in monazite (e.g., Bea & Montero, 1999; Kelly et al., 2012; Pyle & Spear, 2003; Taylor et al., 2016; Yang & Pattison, 2006) and experimental studies including Th in the monazite–melt system (e.g., Rapp et al., 1987; Rapp & Watson, 1986; Stepanov et al., 2012), the behaviour of Th-in-monazite with progressive metamorphism is underexplored. Thus, the changing chemical concentration and zoning of Th and bulk Th content of monazite grains as a function of pressure, temperature and bulk rock composition remains unclear.

Previous studies have successfully linked chemical zoning of Ce or Y in metamorphic monazite to mineral reactions involving garnet, apatite, xenotime and melt (Corrie & Kohn, 2008; Dumond et al., 2015; Kohn & Malloy, 2004; Pyle & Spear, 1999, 2003; Rubatto et al., 2006; Smith & Barreiro, 1990; Wing et al., 2003). However, to date, studies that have focused on Th behaviour in particular are few (Bea & Montero, 1999; Bingen et al., 1996; Skrzypek et al., 2018; Watt, 1995; Williams et al., 2018) and studies reporting Th zoning in monazite have produced seemingly contradictory results (e.g., decreasing Th from core to rim; Kohn & Malloy, 2004; Th-in-monazite is constant or increases with metamorphic grade; Skrzypek et al., 2018; Williams et al., 2018). Recent work by Williams et al. (2018) and Skrzypek et al. (2018), both on low pressure terranes, identified monazite chemical zones in prograde metamorphic sequences. These monazite zones showed a systematic progression of increasing Th from the lowest to highest grade rocks. At Mt Stafford this retention of Th in monazite resulted in the retention of Th in granulite facies rocks despite significant partial melting and interpreted melt loss (Bartoli, 2017; Palya et al., 2011; Williams et al., 2018). In this study, we explore bulk Th and monazite chemistry in the higher-pressure Ivrea–Verbano Zone to explore similarities and differences in the record of monazite formation in these terranes.

Sections of metasedimentary sequences that expose a continuous and well constrained metamorphic gradient are the best targets to investigate monazite composition over a *P–T* range. The Ivrea–Verbano Zone (IVZ) in northern Italy exposes such a sequence along the Val Strona di Omegna. This is an ideal natural laboratory as it (a) provides a continuous metamorphic field gradient from the mid-amphibolite through to granulite facies, with and apparent *P–T* gradient of ~70°C/kbar (Kunz & White, 2019; Redler et al., 2012); (b) contains an abundance of metapelite layers throughout the transect that have arguably consistent chemistry across the solidus (Bea & Montero, 1999; Redler et al., 2012) and thus presents the opportunity to study monazite behaviour without the complexity of significant changes to bulk rock chemistry; and (c) has a well-constrained regional *P–T* framework (Ewing et al., 2013; Kunz et al., 2014; Redler et al., 2012, 2013).

The behaviour of accessory minerals and their trace element compositions in the IVZ was previously studied in the landmark paper by Bea and Montero (1999), details of which are outlined below. However, as informative and revolutionary as the Bea and Montero (1999) study was, it was limited by the resolution of analytical techniques (i.e., whole rock geochemistry and electron probe microanalysis [EPMA]) available at the time. To this end, we revisit the same section of Val Strona di Omegna to add several hundred more data points to the regional bulk rock Th trends reported in Bea and Montero (1999) and examine the micro-scale compositional variations within monazite grains, interpreted within a *P–T*–time framework. The extended data set and greater breadth of interpretation gives greater insight into (a) the preservation (or not) of pre-peak and peak monazite; (b) the relative and changing importance of the two Th substitution mechanisms within natural monazite; and (c) the mineral reactions to which monazite geochronology relates.

2 | GEOLOGICAL SETTING

The Ivrea–Verbano Zone (also known as the Ivrea Zone, IVZ) in the southern Alps, north-west Italy, represents a tilted mid to lower crustal section of the pre-alpine basement (e.g., Bea & Montero, 1999; Brodie & Rutter, 1987; Fountain, 1976; Peressini et al., 2007; Redler et al., 2012,

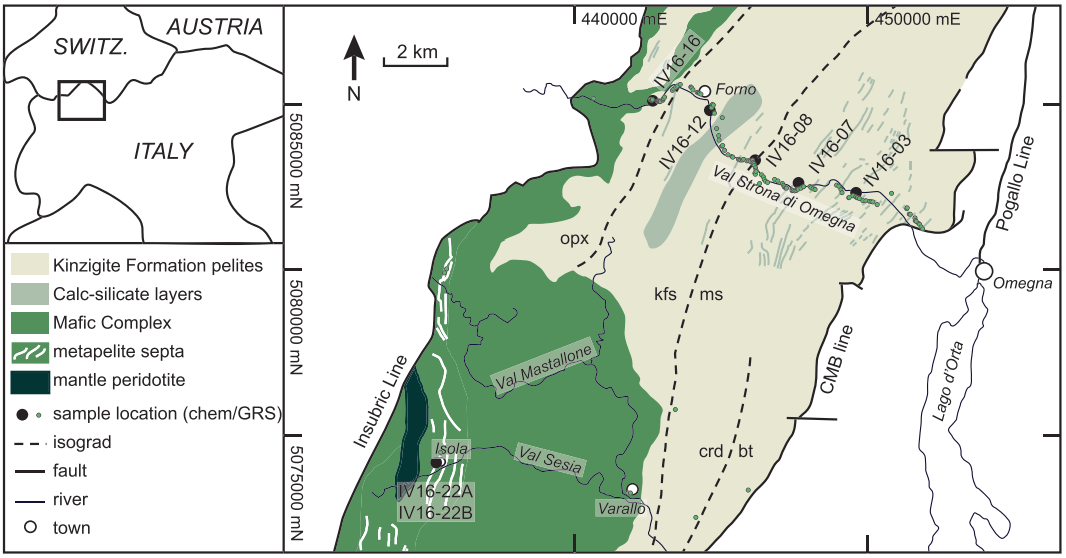

FIGURE 1 Simplified map of the Ivrea–Verbano Zone showing major stratigraphic units (after Bea & Montero, 1999; Redler et al., 2012; Ewing et al., 2013) and locations of samples in this study (see Table 1). Inset: Location of the Ivrea–Verbano Zone. Mineral abbreviations after Kretz (1983) [Colour figure can be viewed at wileyonlinelibrary.com]

2013; Rivalenti et al., 1981; Zingg et al., 1990). The sequence consists of interlayered metabasites and metapelites with subordinate meta-carbonate and calc-silicate layers which together form the Kinzigite Formation (Figure 1). The sequence has a metamorphic field gradient from mid-amphibolite facies rocks (locally known as Kinzigites) in the SE, adjacent to the Cossato–Mergozzo–Brissago (CMB) tectonic line, to granulite facies rocks (locally known as Stronalites) at the base of the section, adjacent to the Insubric line in the west (Figure 1; e.g., Henk et al., 1997; Quick et al., 2003; Redler et al., 2013; Schmid & Wood, 1976; Sills & Tarney, 1984). The sequence is intruded to the SW by a large mafic body ('Mafic Complex', Figure 1), the upper part of which has a narrow contact aureole (~1 km wide) that overprints the regional metamorphic field gradient (Barboza et al., 1999; Barboza & Bergantz, 2000). The minimum *P–T* conditions adjacent to the CMB line, as constrained by thermodynamic forward modelling, are <3.5–7.9 kbar and <640–710°C (Redler et al., 2012). The maximum *P–T* conditions in the continuous metasedimentary sequence, as determined by thermodynamic forward modelling, are >9.5 kbar and >870°C (Kunz & White, 2019; Redler et al., 2012), but higher temperatures up to 1100°C are recorded by Zr-in-rutile thermometry in the slivers of metapelites ('septa') within the Mafic Complex (Ewing et al., 2014; Pape et al., 2016). The metamorphic field (thermal) gradient in Val Strona di Omegna is approximately 70°C/kbar based on the published *P–T* results (Kunz & White, 2019; Redler et al., 2012). Forward thermodynamic modelling of granulite facies samples from the IVZ indicates that metapelites produced up to 25–30% melt which was progressively extracted (Redler et al., 2013).

Remnants of regional metamorphism related to the Variscan Orogeny in the IVZ have been dated to circa 320–300 Ma (Ewing et al., 2013; Kunz et al., 2018; Vavra et al., 1999). The Mafic Complex intruded the sequence shortly afterwards. The main pulse of the Mafic Complex was dated at 288 ± 4 Ma by Peressini et al. (2007), and a recent ID–TIMS study constrains the main felsic and mafic magmatism to a short period between 286 and 282 Ma (Karakas et al., 2019). Minor magmatic activity occurred from circa 300 to 270 Ma (Klötzli et al., 2014; Peressini et al., 2007). The majority of U–Pb ages (zircon and monazite) in the pelitic rocks constrain regional heating to amphibolite and granulite facies conditions to the Permian, that is, 290–270 Ma (Ewing et al., 2013; Guergouz et al., 2018; Henk et al., 1997; Kunz et al., 2018; Vavra et al., 1999). Geochronology from the IVZ suggests that the Mafic Complex formed during a sequential emplacement, providing significant thermal energy required for the granulite facies metamorphism of the Kinzigite Formation (Ahrendt et al., 1989; Baker, 1990; Barboza et al., 1999; Peressini et al., 2007). Relatively high temperatures may have been maintained until cooling below ~ 550°C in the Jurassic (175–160 Ma), as constrained by rutile geochronology (Ewing et al., 2015). Rifting to the west of the IVZ during the late Permian to Jurassic may have resulted in some fluid influx within the Mafic Complex (Vavra et al., 1999; Vavra & Schaltegger, 1999). Tilting of the IVZ into its current steeply inclined orientation is suggested to have begun during the Jurassic (Wolff et al., 2012) and

continued during the Oligocene as part of the Alpine Orogeny (e.g., Handy et al., 1999).

The behaviour of accessory minerals in the IVZ was previously studied by Bea and Montero (1999), who documented the chemistry of metapelites, metabasites and leucosomes in Val Strona di Omegna, as well as the abundance, habit, microstructural location and chemistry of the four common accessory minerals in these rocks: monazite, xenotime, apatite and zircon. Progressive changes to accessory mineral composition documented in that study demonstrate that reactions between accessory, major minerals and, where present, melt were continuous throughout the metamorphic sequence (see also Corrie & Kohn, 2008; Kohn & Malloy, 2004). Monazite in the sequence was not consumed by major mineral-forming reactions, retaining a similar modal abundance with increasing metamorphic grade, and did not completely dissolve into melt even at high temperatures, as evidenced by its presence in the residual granulites at the highest metamorphic grade. Bea and Montero (1999) reported that the proportion of high-Th/U monazite increases with metamorphic grade, and its predominant location at grain boundaries suggested growth in the presence of melt. Bea and Montero (1999) observed that metapelitic rocks throughout the sequence have approximately the same average concentration of LREE and Th regardless of metamorphic grade. Similarly, the metabasites do not show any perceptible change in Th concentration with increasing metamorphic grade. The study concluded that chemical changes associated with metamorphism and partial melting did not significantly change heat production in the lower crust. The heat production of the Val Strona metapelites was recently investigated by Alessio et al. (2018), who showed empirically that the heat production in the Ivrea–Verbano Zone was equivalent in sub- and supra-solidus rocks.

3 | MINERAL ASSEMBLAGES AND TEXTURES IN METAPELITES

The IVZ is split into three zones based on metamorphic assemblages: the Kinzigite zone, a transition zone and the Stronalite zone, which broadly correspond to mid- and upper-amphibolite and granulite facies, respectively (Bea & Montero, 1999; Redler et al., 2012; Schnetger, 1994). Amphibolite facies metapelites in the Kinzigite zone are folded micaschists with variable proportions of biotite, muscovite, fibrolitic sillimanite, garnet, plagioclase and quartz (Figure 2 a,b). At the lowest grade, micaschists contain leucocratic patches with a high proportion of muscovite and plagioclase that are almost completely devoid of biotite (Figure 2a; e.g., Bea & Montero, 1999). These leucocratic patches were described by Bea and

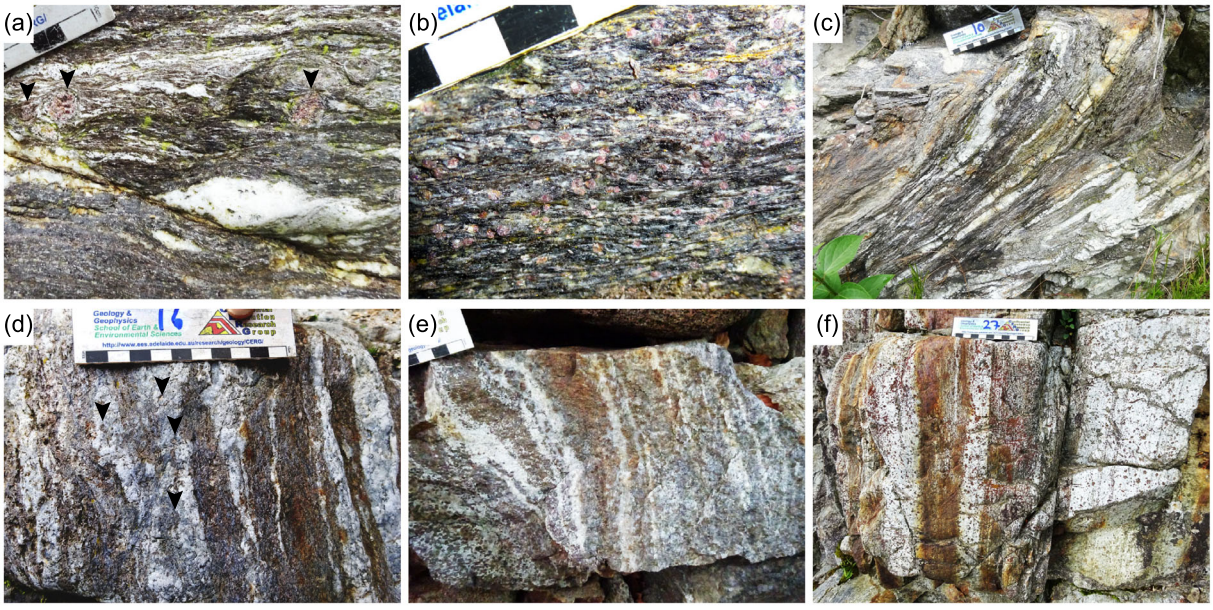

FIGURE 2 Field relations from Val Strona di Omegna (a)–(e) and Val Sesia (f), in order of increasing metamorphic grade. Scale bar graduations 10 mm. (a) Micaschist with garnet porphyroblasts and muscovite rich leucocratic patches (lower amphibolite; IV16-03A). Arrows indicate garnet porphyroblasts; (b) Micaschist with abundant garnet (lower amphibolite; IV16-07); (c) folded micaschist with muscovite-poor leucocratic patches (upper amphibolite; IV16-08); (d) garnet–sillimanite–biotite gneiss. Arrows indicate peritectic garnet (granulite; IV16-12); (e) garnet–sillimanite gneiss (biotite absent, granulite; IV16–16); (f) layered residual metapelite in UHT septa. Light bands are mainly plagioclase–garnet, dark bands are rich in garnet and sillimanite (UHT granulite; IV16-22A/B) [Colour figure can be viewed at wileyonlinelibrary.com]

Montero (1999) as hydrothermal mobilizates. Garnet at the lowest metamorphic grade occurs as rare isolated porphyroblasts, wrapped in a fabric of biotite and muscovite (Figure 2a). With increasing metamorphic grade, garnet becomes more abundant and generally smaller in size (Figure 2b). The transition zone represents the change from amphibolite to granulite facies assemblages and extends from the K-feldspar-in isograd in the metapelites to the orthopyroxene-in isograd in the metabasites (Bea & Montero, 1999; Redler et al., 2012). In this zone, the metapelitic rocks change from micaschists to gneisses, accompanied by an overall decrease in the modal proportion of biotite and increase in the modal proportion of garnet, sillimanite and leucosome (Figure 2c). In the granulite facies zone (Stronalite) the metapelites consist primarily of garnet, plagioclase, K-feldspar, prismatic sillimanite, biotite and quartz, with accessory rutile, ilmenite and graphite. The modal proportion of biotite decreases with metamorphic grade, in an inverse relationship with the increase in the number and volume of leucosomes preserved in the rocks and modal abundance of peritectic garnet (Figure 2d). Whole rock geochemistry and phase equilibria modelling by Redler et al. (2013) shows that the unmelted mid-amphibolite facies rocks in the IVZ can be considered as protolith compositions for the rocks at higher metamorphic grades and that melt production in the granulite facies rocks reached a maximum of approximately 25–30 mol. %. Within the Mafic Complex exist several septa of metapelitic rocks that were metamorphosed to ultra-high temperature granulite (UHT; >900°C) conditions and have mineral assemblages containing abundant garnet, sillimanite, plagioclase (sometimes perthitic), rutile and virtually no biotite (Figures 1 and 2f; e.g., Ewing et al., 2013).

4 | SAMPLE SELECTION

Representative metapelite samples of the IVZ were collected along the well exposed traverse in Val Strona Di Omegna (Val Strona; Figures 1 and 2). This part of the sequence is the best exposed, most continuous, easily accessible and the furthest removed from the overprinting effects of the Mafic Complex in the SW, thus is the best place to study the regional metamorphic trend. The Val Strona sequence has been extensively investigated in terms of petrology and geochronology (e.g., Bea & Montero, 1999; Ewing et al., 2013, 2014; Kunz et al., 2018; Kunz & White, 2019; Peressini et al., 2007; Redler et al., 2012; Redler et al., 2013, and references therein), allowing direct comparison of the new results with previous studies. Of the 31 samples collected and investigated for bulk rock composition in this study, seven were selected for detailed textural and mineral analysis (Table 1). Three amphibolite facies and two granulite facies metapelites are from Val Strona; two samples are UHT metapelite from septa within the Mafic Complex from the locality of Isola in Val Sesia (Figures 1 and 2f). One UHT sample represents the restite with abundant garnet (IV16-22A) whereas the other is more leucocratic (IV16-22B). Thin sections were cut in the same orientation for all samples, perpendicular to foliation and parallel to lineation.

5 | METHODS

5.1 | Whole-rock geochemistry

Whole-rock geochemical analyses of all collected samples were undertaken to determine similarity of chemical

TABLE 1 Samples and locations. Samples listed in increasing grade order, refer to Figure 1

Sample	Metm. Grade	Rock type	Mineralogy	Location
IV16–03A	Amphibolite	Pelite with vein	Bt–ms–pl–grt–qtz Mnz–apt–xtm–zrn	0450804 mE 5083388mN
IV16–07	Amphibolite	Pelite	Bt–sil–pl–grt–ms–qtz Mnz–apt–xtm–zrn–gr	0448640 mE 5083912mN
IV16–08	Amphibolite	Pelite	Bt–ms–pl–grt–qz–sil Mnz–apt–xtm–zrn–gr	0446706 mE 5084125mN
IV16–12	Granulite	Pelite	Bt–ms–pl–grt–sil–ru–qz Mnz–apt–xtm–zrn–gr	0445135 mE 5086576mN
IV16–16	Granulite	Pelite Restite	Bt–pl–kfs–grt–sil–ru–qz–gr Mnz–apt–xtm–zrn	0442972 mE 5087044mN
IV16-22A	UHT	Pelite Leucosome	Sil–pl–grt–qtz–rt–ilm Mnz–apt–xtm–zrn–aln–chl	0435591 mE 5074755mN
IV16-22B	UHT	Pelite Restite	Grt–sil–pl–qtz–rt–ilm Mnz–apt–xtm–zrn–aln–chl	0435591 mE 5074755mN

Note: Metamorphic grade after Redler et al. (2012). Locations are in UTM coordinates, zone 32 T, using the WGS84 datum. Mineral abbreviations after Kretz (1983). Metm., metamorphic; UHT, ultra-high temperature granulite. Vein in IV16-03A comprises 10% of thin section.

composition between samples as well as to quantify bulk rock concentrations of heat producing elements. Whole-rock geochemical analyses were undertaken by Wavelength Dispersive X-ray Fluorescence spectrometry at the Department of Earth and Environment, Franklin and Marshall College, Lancaster PA, USA. Major elements were analysed on fused disks prepared using a lithium tetraborate flux. Whole rock geochemistry for all collected samples is provided in Table S1. Element (ppm) and oxide (wt%) concentrations from whole-rock geochemistry are herein denoted in the form Th_WR and CaO_WR, respectively (e.g., trace and major elements).

5.2 | In-field gamma-ray spectrometry

Handheld gamma ray spectrometry (GRS) data for the Ivrea–Verbano Zone were published in Alessio et al. (2018), which contains the full data set and methods for this technique. Analyses were collected from transects of the IVZ, predominantly in Val Strona Di Omegna, from lowest to highest metamorphic grade, with multiple analyses collected at each location to account for the natural heterogeneity of sequences in outcrop (Figure 3). Thorium concentrations obtained from in-field GRS data are denoted Th_GRS and are cast as ppm.

5.3 | Mineral liberation analysis (MLA)

Entire thin sections were mapped for monazite, xenotime, zircon, allanite and apatite at Adelaide Microscopy, the University of Adelaide, using a FEI Quanta600 Scanning Electron Microscope (SEM) with automated MLA software (Gu, 2003). Full detail of the MLA procedure is detailed in Williams et al. (2018).

5.4 | EPMA

Qualitative mapping and quantitative analyses of monazite chemistry were performed at Adelaide Microscopy, the University of Adelaide, using a Cameca SXFive electron microprobe following the method described in Williams et al. (2018). Pb was not analysed for any samples herein to reduce individual spot analysis time. Average detection limits for each element (Table 4) were calculated from the individual detection limits on all point analyses in the study. Monazite wt% oxide and cation data for 4-oxygen monazite from EPMA will be denoted in the form ThO_2_mnz and Th^{4+}_mnz, respectively.

5.5 | Laser ablation–inductively coupled plasma–mass spectrometry (LA–ICP–MS)

In situ U–Pb dating and trace element concentrations of monazite were quantified by Laser Ablation ICP–MS

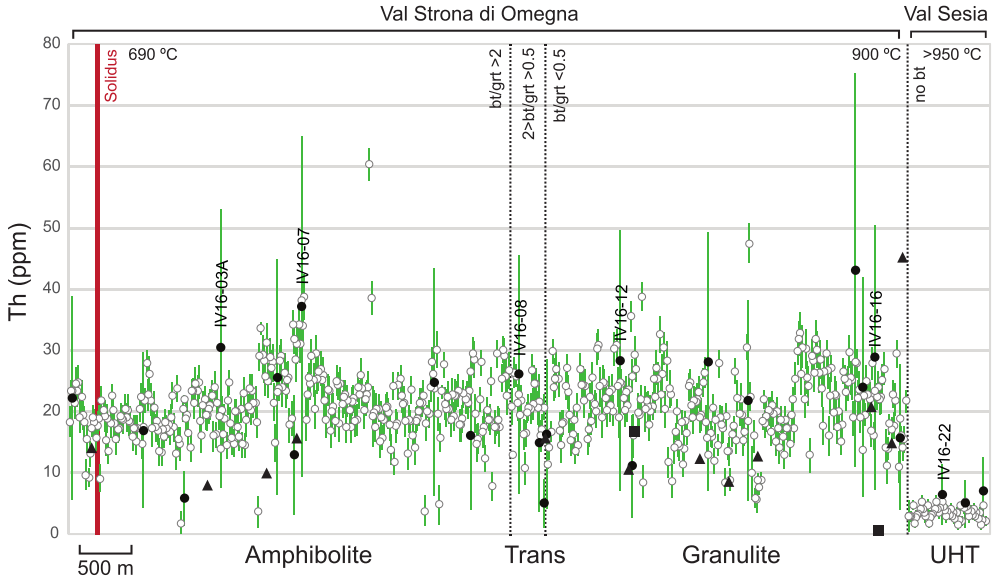

FIGURE 3 Th_GRS (open circles) and Th_WR (filled circles) concentrations in the Ivrea–Verbano Zone as a function of metamorphic grade. Th_GRS concentrations are from Alessio et al. (2018). Th_WR concentrations are presented in Table S1. Solid red line indicates the in-field location of the solidus, black dotted lines indicate facies transitions, as defined by Bea and Montero (1999) on the basis of modal biotite/garnet (bt/grt). Error bars are 2 sigma: Th_GRS errors calculated from machine errors, Th_WR errors calculated from standard data. Pressure–temperature estimates from Redler et al. (2013) and Ewing et al. (2013). Whole rock Th concentrations from Bea and Montero (1999) and Guergouz et al. (2018) indicated by black triangles and squares respectively. Location of samples shown in Figure 1. Trans, transition zone; UHT, ultra high temperature granulite (septa) [Colour figure can be viewed at wileyonlinelibrary.com]

at Adelaide Microscopy, the University of Adelaide. Analysis spot locations were selected based on zoning identified in EPMA maps of grains, with spots located within specific chemical zones where possible adjacent to EPMA point analyses. Ablation of monazites was performed in situ with a beam diameter of 13 μm. A common Pb correction was applied using the 'VizualAge_UcomPbine' Data Reduction Scheme (Chew et al., 2014) in the programme Iolite (Paton et al., 2011) which applies a common Pb correction following the ^{207}Pb method. Detailed LA–ICP–MS methods are described in Appendix S2 and uncorrected data are provided in Table S3.

6 | RESULTS

6.1 | Bulk rock composition

Whole rock Th concentrations measured by X-ray Florescence (Th_WR) for all samples are in the range 5–43 ppm, within the range of whole rock Th measured by in-field GRS and other published analyses from Val Strona (Figure 3, Table S1). The chemistry of the amphibolite and granulite facies samples (Table 2) is equally spread in the AFM and Al_2O_3–(CaO + Na_2O)–K_2O diagrams (Figure 4a,b) regardless of metamorphic grade. Amphibolite and granulite facies samples with similar (high Al, low Ca) compositions were selected for further analysis. This composition was chosen due to its propensity to form and retain monazite, enabling the largest *P–T* range over which to study monazite chemistry (e.g., Spear, 2010; Spear & Pyle, 2010). In particular, monazite in these rock compositions exists well above the solidus, enabling study of monazite–melt interactions. The UHT samples have distinctly lower K_2O (Figure 4b) than amphibolite and granulite facies samples. Samples IV16-22A and IV16-22B were selected for further analysis as they are the least weathered of the UHT samples. In addition to having lower K_2O than other samples selected for analysis, these samples also have significantly higher CaO and Na_2O (Figure 4b). Whether the UHT rock chemistry reflects the primary chemistry of the metasediments is unclear. However, CaO- and Na2O-rich metasediments are reported from within the Ivrea section (Figure 4b; Bea & Montero, 1999; Guergouz et al., 2018; Schnetger, 1994).

In-field GRS data (Th_GRS) from IVZ metapelites (Figure 3, data from Alessio et al., 2018) shows no change in the range of Th ppm concentrations between amphibolite and granulite facies rocks with peak temperatures up to approximately 900°C. Analyses from the UHT septa at Isola (peak temperatures >950°C) have significantly lower Th_GRS than lower-temperature granulite facies metapelites (Figure 3). The average Th_GRS ppm for the amphibolite, granulite and UHT samples are 21 ± 5 ($n = 306$), 20 ± 6 ($n = 249$) and 3 ± 1 ($n = 54$), respectively (errors are 1 s.d.). Analyses for each facies fall in the ranges 3–34, 3–31 and 1–5 ppm, respectively (see Alessio et al., 2018).

6.2 | Monazite petrography and volume proportions

Monazite occurs in all seven samples investigated, encompassing amphibolite facies to UHT conditions. Accessory mineral textural locations are shown in Figure 5, volume proportions and grain characteristics are shown in Figure 6 and EPMA monazite grain images are shown in Figure 7. Further detailed accessory mineral petrography is available in Appendix S4. In the amphibolite facies samples, monazite occurs predominantly within the matrix, included within or at the grain boundaries of biotite (Figure 5a) and K-feldspar (Figure 5a,b), and aligned with the fabric. Monazite rarely occurs as very small grains included in garnet poikiloblasts in sample IV16-07 (e.g., Figure 5b).

In granulite facies sample IV16-12, monazite occurs within the matrix adjacent to sillimanite (Figure 5c), plagioclase (Figure 5d) and biotite (Figure 5d), and rarely at sillimanite–ilmenite/rutile and garnet-sillimanite grain boundaries (Figure 5c,d). In granulite facies sample IV16-16, monazite most commonly occurs within leucosomes (Figure 5e,f) or as inclusions in garnet (Figure 5f). Allanite in the granulite facies samples occurs as patchy aggregates, commonly with Th-orthosilicate, at grain boundaries and as discontinuous rims on large monazite grains (Figure S4). In the UHT samples, monazite occurs adjacent to quartz, K-feldspar, plagioclase and sillimanite (Figure 5g,h), and rarely as inclusions in or adjacent to garnet (Figure 5g).

Monazite maximum grain size increases from amphibolite facies to granulite facies, then decreases sharply in the UHT samples (Table 3). Monazite volume proportions ('modes') are in the range 0.001–0.047 vol.% (Table 3, Figure 6). Monazite modes increase slightly through the amphibolite facies (0.037, 0.045 and 0.047 vol.%, Table 3) then decrease through the granulite facies (0.039 and 0.027 vol.%). Granulite facies monazite is affected by two retrograde reactions, producing aggregates of (1) allanite and Th-orthosilicate and

TABLE 2 Whole rock geochemistry for studied samples from the Ivrea–Verbano zone

	Amphibolite			Granulite		UHT	
	IV16-03A	**IV16–07**	**IV16–08**	**IV16–12**	**IV16–16**	**IV16-22A**	**IV16-22B**
Major elements (wt%)							
SiO_2	49.18	51.88	56.96	57.00	54.75	57.75	46.53
TiO_2	1.34	1.16	1.16	1.19	1.56	1.31	1.83
Al_2O_3	28.66	28.54	22.88	22.86	24.58	18.16	23.18
Fe_2O_3T	12.18	12.57	9.79	10.57	12.71	11.33	16.16
MnO	0.14	0.13	0.19	0.26	0.13	0.17	0.26
MgO	3.48	1.69	2.91	2.69	3.87	4.64	5.47
CaO	0.15	0.56	0.47	1.22	0.46	2.66	2.82
Na_2O	0.46	0.74	1.21	0.73	0.57	2.27	2.22
K_2O	4.29	2.87	3.93	3.19	1.39	1.51	1.23
P_2O_5	0.05	0.06	0.17	0.15	0.05	0.09	0.06
Total	99.93	100.20	99.67	99.86	100.07	99.89	99.76
LOI	1.62	1.88	2.41	2.80	2.00	1.38	1.85
Fe_2O_3	10.37	8.53	7.96	6.68	10.13	6.32	10.74
FeO	0.66	3.09	0.94	3.15	1.45	4.31	4.22
Trace elements (ppm)							
Rb	283	228	233	147	48	13	14
Sr	62	205	125	133	132	365	333
Y	16	45	28	39	58	89	127
Zr	161	203	189	185	195	242	311
V	203	173	179	238	226	187	281
Ni	72	69	76	104	65	72	51
Cr	160	165	166	209	178	192	199
Nb	26	37	25	18	24	20	41
Ga	40	45	32	32	38	20	27
Cu	96	26	36	60	41	65	59
Zn	191	205	143	165	149	189	171
Co	42	37	31	38	45	38	55
Ba	610	399	475	706	558	863	642
La	30	43	26	40	36	40	26
Ce	62	76	56	83	72	73	55
U	n/d	n/d	n/d	n/d	n/d	n/d	n/d
Th	31	37	25	28	29	7	5
Sc	22	18	17	14	19	18	34
Pb	1	9	7	13	1	6	11

Note: FeO and Fe_2O_3 determined by titration.

(2) LREE-rich apatite and cheralite (Appendix S4; Bea & Montero, 1999). These aggregates are too fine grained to estimate mineral proportions using the MLA method but indicate that the proportion of monazite in the granulite facies samples was somewhat higher than that preserved. The UHT samples (IV16-22A, IV16-22B) have the lowest mode of monazite of all samples (0.004 and 0.001 vol.% respectively).

Based on our estimates from the Val Strona di Omegna section, the zircon mode is variable but may

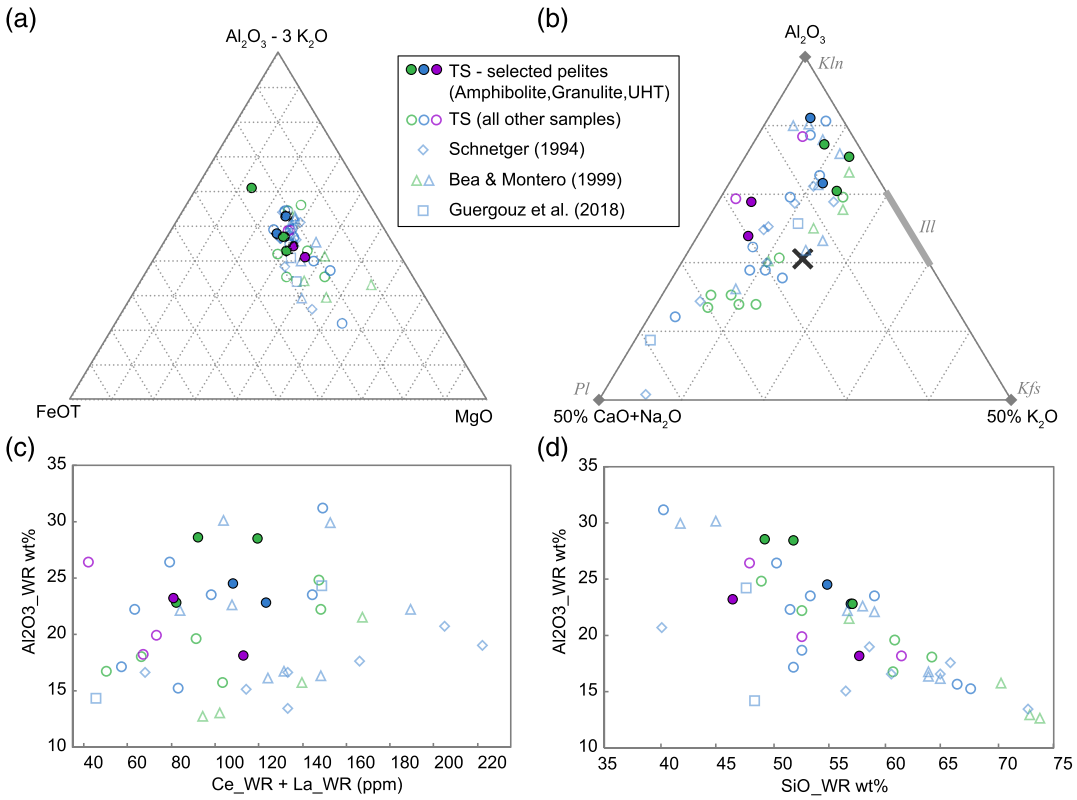

FIGURE 4 Whole-rock geochemistry from the Ivrea–Verbano zone metapelites of this study. (a) Al_2O_3–FeO (total)–MgO (AFM) diagram. (b) Al_2O_3–CaO + Na_2O–K_2O diagram after Janots et al. (2006). Shaw's average pelite shown with grey cross (Shaw, 1956). Ill, Illite, Kln, Kaolinite, Kfs, K-feldspar, Pl, plagioclase. (c) Al_2O_3_WR versus Ce_WR + La_WR. (d) Al_2O_3_WR versus SiO_2_WR. See Table S1 for whole rock geochemical analyses [Colour figure can be viewed at wileyonlinelibrary.com]

increase slightly with metamorphic grade (Figure 6 and Table 3). Xenotime mode is variable within the amphibolite facies samples and decreases sharply in the granulite facies and UHT samples. Apatite proportion is the most variable and has maximum volume proportion in the upper amphibolite facies (Figure 6a). Allanite occurs in cracks in garnet in sample IV16-03A and is virtually absent in the other amphibolite facies samples (Figure 6a). Allanite occurs as fine-grained aggregates on monazite grain boundaries in leucocratic parts of all granulite and UHT samples, with greatest volume proportion in IV16-16. Volume estimates based on MLA maps confirm that garnet volume proportion broadly increases with metamorphic grade (Figure 6b).

6.3 | Monazite composition

Monazite has been separated into nine distinct chemical zones based on EPMA map and point analysis data, summarized in Tables 4 and 5. Zones were correlated between grains in the same sample, and also between samples, according to texture and chemical composition and in particular: (a) the regular and recurring spatial organization of distinct zones in EPMA maps (Figure 7); and (b) the identification of distinct populations in divariant scatter (Harker) plots of EPMA point data (Th, Ce, Y, Ca Figure 8a). Monazite zones 1–4 (Z1–Z4) occur in the amphibolite facies samples, zones 5–7 (Z5–Z7) occur in the granulite facies samples and zones 8 and 9 (Z8, Z9) occur in the UHT samples. Three of the nine zones (Z4, Z5, Z7) occur solely within single samples, with the remaining six zones occurring in two or more samples.

Monazite Z1 is a Th-poor and REE-rich zone with moderate Y (Figure 8). Monazite Z1 occurs within the cores of monazite grains in samples IV16-03A and IV16-08 and is surrounded by Z2 and Z3 monazite (Figure 7). Monazite Z2 is a moderate Th, Y-poor zone and Z3 is a moderate Th, Y-rich zone (Figure 8). Zones 2 and 3, found in samples IV16-03A, IV16-07 and IV16-08, consistently show a core–mantle relationship,

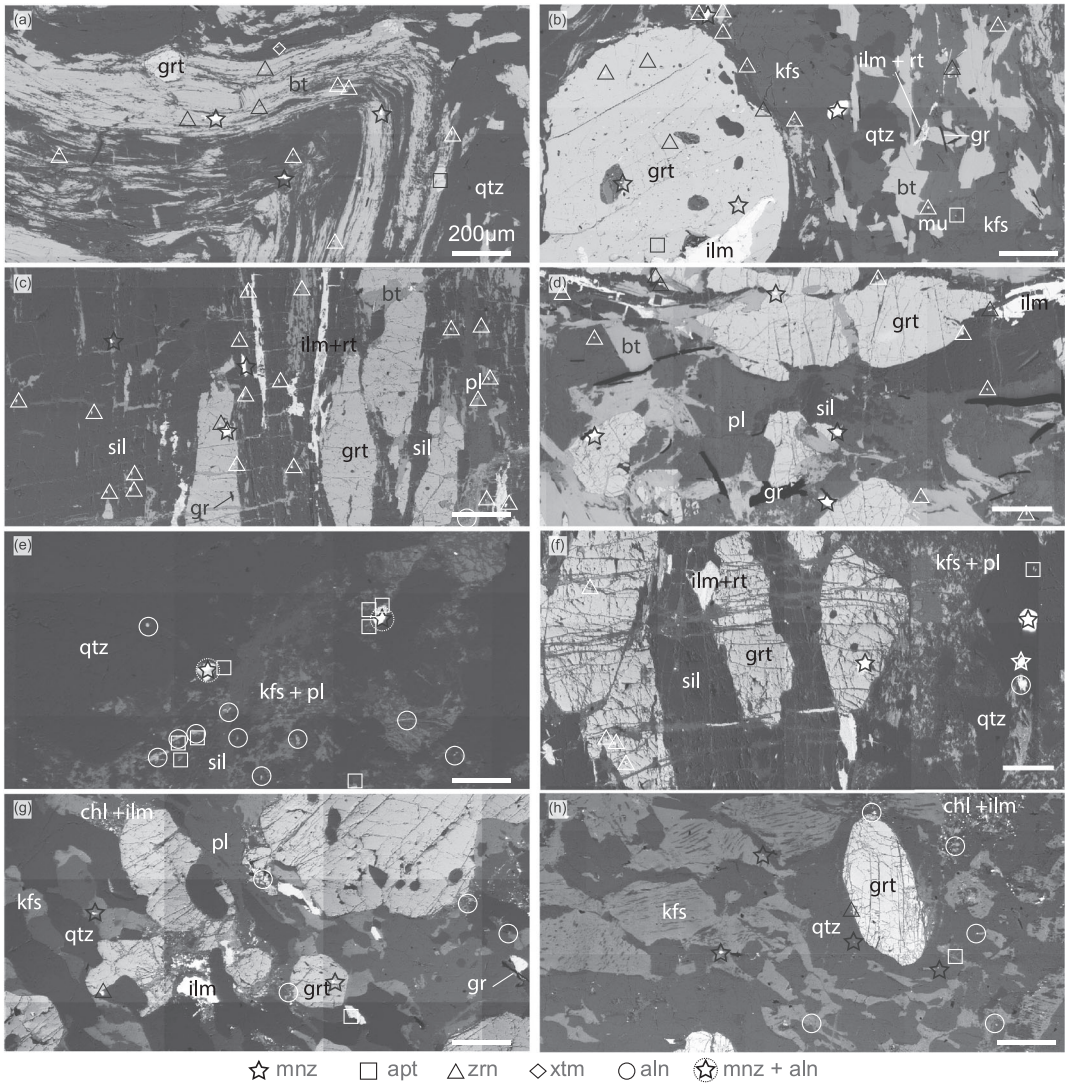

FIGURE 5 Representative backscattered electron photomicrographs indicating microstructural setting of monazite and other accessory minerals. (a) IV16-08; monazite preferentially distributed along the biotite fabric. (b) IV16-07; monazite within matrix and included in garnet. (c) IV16-12; mnz at sillimanite–garnet grain boundary and aligned with sillimanite–biotite fabric. (d) IV16-12; monazite included in garnet and plagioclase, and at garnet-plagioclase and garnet-biotite grain boundaries. (e) IV16-16; monazite with allanite rims in leucosome. (f) IV16-16; monazite included in quartz and garnet. (g) IV16-22A; monazite included in K-feldspar and garnet. (h) IV16-22B; monazite in K-feldspar and quartz in leucosome. (a–h) Mineral abbreviations after Kretz (1983)

with Z2 internal to Z3. The width of Z3 rims increases with metamorphic grade (Figure 7). Zone 4 is a very Y-rich zone with moderate Th and low LREE (Figure 8). Zone 4 occurs only in sample IV16-03A as isolate grains with embayed edges within a leucocratic vein (see also Bea & Montero, 1999). Zone 5 is a moderate Th, moderate Y, and moderate REE zone (Figure 8). Zone 5 occurs as cores of grains and rarely as isolate grains in granulite facies sample IV16–12. Zone 5 has Y between that of Z2 and Z3 (Figure 8a) and is therefore defined as a distinct monazite zone. Zone 6 is a moderate Th, low–moderate Y, and moderate REE zone (Figure 8). Zone 6 occurs in samples IV16–12 and IV16–16, in the former as rims around Z5 and in the latter as cores of grains. Zone 7 is a moderate Th, Y- and HREE-poor and LREE-rich zone (Figure 8). Zone 7 occurs in sample IV16–16 as narrow, discontinuous rims around Z6. Monazite Z8 is a very Th-rich, Y- and REE-poor zone and Z9 is a very LREE-rich, Th- and Y-poor zone (Figure 8). Monazite Z8 occurs within and adjacent to garnet grains in both UHT samples and Z9 occurs in the matrix of the UHT samples. Monazite zone 9 also occurs within garnet grains along fractures connected to the matrix. There are no additional microstructural controls on the appearance of other monazite zones (Z1–Z3, Z5–Z8) other than described above.

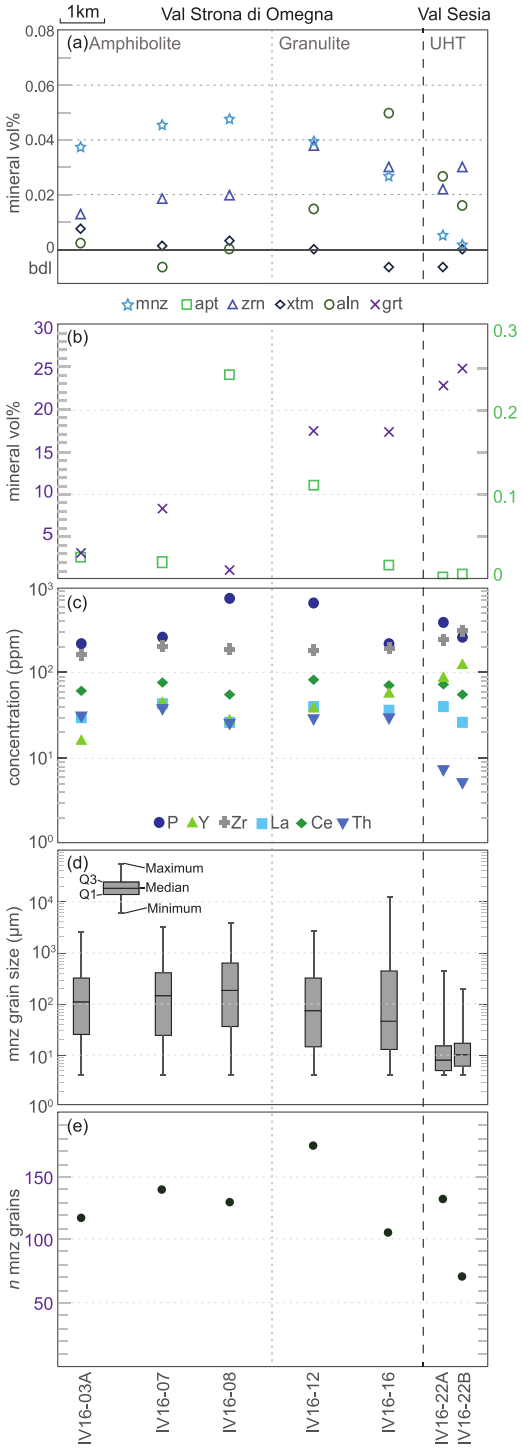

FIGURE 6 Mineralogical and chemical variation across metamorphic grade. Distance scale (*x* axis) shows distance between projected location of samples onto a linear transect of Val Strona di Omegna, increasing in metamorphic grade from left to right. Dashed line indicates break in section. IV16-22A and IV16-22B were collected approximately 1 m apart in the outcrop of Val Sesia. Note logarithmic scale for (c) and (d). Uncertainty in measurements represented by the size of markers. (a) Volume proportions of accessory minerals (as vol.%), calculated from point counting of MLA maps. bdl, below detection limit (10^{-6} vol.%). Note that peak monazite proportions for IV16-12 and IV16-16 was higher than that preserved in the samples (see Section 6.2). (b) Volume proportions of garnet and apatite (as vol.%) calculated from point counting of MLA maps. Garnet scale on left of diagram, apatite scale on right. (c) Whole rock concentrations of P and selected trace elements, as element ppm. (d) Boxplots of monazite grain size determined from MLA mapping. Boxplots show dispersion of data, the interquartile range and median values for each element. Q1, quartile 1; Q3, quartile 3. (e) Number of monazite grains in each sample (thin section) determined from MLA maps. (a–e) aln, allanite; apt, apatite; gt, garnet; mnz, monazite; xtm, xenotime; zrn, zircon [Colour figure can be viewed at wileyonlinelibrary.com]

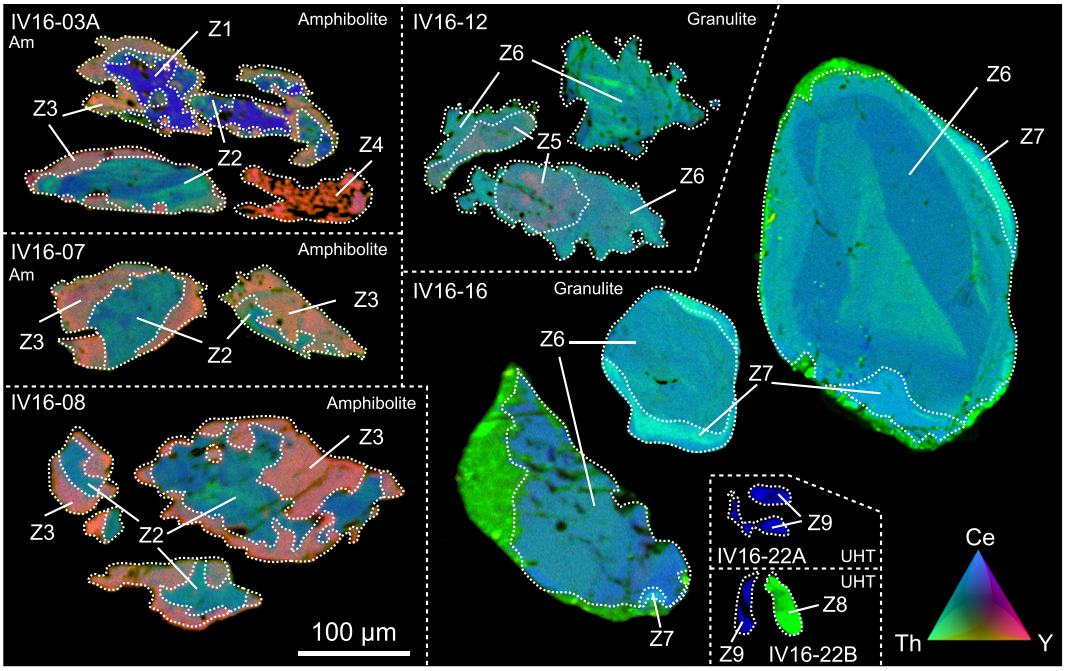

FIGURE 7 Representative composite EPMA maps of element concentrations in monazite from the Ivrea–Verbano Zone metapelites. Images are composite qualitative maps of thorium, cerium and yttrium with the three element maps overlain. Green channel represents ThO_2 in the range 0–20.3 wt%, blue represents Ce_2O_3 in the range 0–33.9 wt% and red represents Y_2O_3 in the range 0–3.4 wt%. Colour scale shows the relative proportions of the elements Th, Ce and Y in each grain, scaled to highlight differences in chemistry between monazite zones. Z1–Z9 refer to monazite zones described in text. Bright green areas in IV16-16 represent intergrowths of allanite and Th-orthosilicate [Colour figure can be viewed at wileyonlinelibrary.com]

TABLE 3 Modal proportions of accessory minerals (vol.%) and grain characteristics in IVZ samples determined from point counting of MLA maps

	Volume proportion (vol.%)							*Grain size (µm)*		
Sample	**Mnz**	**Ap**	**Zrn**	**Xtm**	**Grt**	**Aln**	***n***	**Ave**	**SD**	**Max**
IV16-03A	0.0367	0.0238	0.0128	0.0078	3.00	0.0022	114	308	497	2613
IV16–07	0.0449	0.0184	0.0182	0.0016	8.21	n.d.	137	362	564	3184
IV16–08	0.0472	0.2413	0.0195	0.0034	1.00	2.10×10^{-6}	129	426	595	3890
IV16–12	0.0389	0.1097	0.0375	3.87×10^{-5}	17.37	0.0147	174	264	431	2646
IV16–16	0.0266	0.0149	0.0300	n.d.	17.26	0.0489	113	595	1520	12504
IV16-22A	0.0045	0.0005	0.0217	n.d.	22.62	0.0265	133	18	42	438
IV16-22B	0.0010	0.0041	0.0297	3.86×10^{-5}	24.64	0.0159	71	21	32	197

Note: Volume proportion detection limit is 10^{-6} vol.%. n.d. not detected; mnz, monazite; ap, apatite; zrn, zircon; xtm, xenotime; grt, garnet; aln, allanite; *n*, number of monazite grains.

Th varies from <0.0003 to 0.19 atoms per formula unit (APFU; Table 5 and Figure 8a,b). It increases from monazite Z1 to Z2, then it is effectively constant in the remaining amphibolite facies zones and in granulite facies samples (Z5–Z7). Monazite Z8 in UHT samples has the highest Th concentration of all zones and Z9 the lowest. Y data show a peak in the amphibolite facies samples (maximum of 0.07 APFU Y in Z4), intermediate Y concentration in the core of the granulite facies monazite Z5 (0.01–0.03 APFU), and low Y concentrations (<0.0008–0.02 APFU) through the granulite facies and UHT samples (Figures 7 and 8). There is a similar, although more subtle, trend in Gd and U concentrations: higher contents are found in the rims of monazite grains of amphibolite facies samples or cores of monazite grains of granulite facies samples (Z1–Z5). ΣLREE and Ca have

TABLE 4 Representative EPMA analyses of monazite

Mnz zone		**Z1**	**Z2**	**Z3**	**Z4**	**Z5**	**Z6**	**Z7**	**Z8**	**Z9**
Sample		03A	07	08	03A	12	12	16	22B	22A
Grain		Mnz 6	Mnz 2	Mnz 9	Mnz 4	Mnz 5	Mnz 9	Mnz 1	Mnz 5	Mnz 8
Analysis	**d.l.**	23–6	40–6	31–3	22–4	54–2	58–2	104–6	66–3	120–1
SiO_2	0.02	0.21	0.38	0.12	0.14	0.33	0.22	0.82	1.98	0.26
CaO	0.01	0.25	0.97	1.09	0.71	0.90	1.02	0.37	2.56	0.13
Y_2O_3	0.04	0.60	b.d.l.	1.89	3.32	0.62	0.12	b.d.l.	0.12	0.06
La_2O_3	0.04	13.42	15.55	14.64	14.64	14.87	14.72	12.85	11.64	16.23
Ce_2O_3	0.04	32.18	29.22	28.63	28.19	29.56	30.09	32.79	23.23	33.30
Pr_2O_3	0.15	3.81	3.23	3.07	3.15	3.22	3.25	4.00	2.62	3.65
Nd_2O_3	0.15	13.87	11.67	10.65	11.06	11.40	12.32	13.61	9.63	13.42
Sm_2O_3	0.16	2.18	2.05	1.68	1.84	1.76	1.67	0.92	1.09	1.12
Gd_2O_3	0.17	1.62	1.16	1.23	1.71	0.92	0.65	0.23	0.38	0.33
ThO_2	0.03	0.75	4.35	4.50	2.12	4.28	4.53	4.37	17.63	b.d.l.
UO_2	0.01	0.07	0.48	0.56	0.68	0.27	0.23	0.05	0.04	0.06
P_2O_5	0.05	31.38	30.59	31.85	31.51	31.21	31.10	29.59	28.40	31.00
Total		**100.35**	**99.67**	**99.93**	**99.07**	**99.35**	**99.94**	**99.60**	**99.33**	**99.55**
Si^{4+}		0.008	0.015	0.005	0.005	0.013	0.009	0.032	0.078	0.010
Ca^{2+}		0.010	0.040	0.045	0.029	0.037	0.042	0.016	0.108	0.005
Y^{3+}		0.012	b.d.l.	0.038	0.068	0.013	0.002	b.d.l.	0.003	0.001
La^{3+}		0.189	0.223	0.205	0.206	0.211	0.209	0.186	0.169	0.231
Ce^{3+}		0.451	0.415	0.398	0.394	0.416	0.424	0.471	0.335	0.471
Pr^{3+}		0.053	0.046	0.043	0.044	0.045	0.046	0.057	0.038	0.051
Nd^{3+}		0.190	0.162	0.144	0.151	0.157	0.169	0.191	0.136	0.185
Sm^{3+}		0.029	0.027	0.022	0.024	0.023	0.022	0.012	0.015	0.015
Gd^{3+}		0.021	0.015	0.015	0.022	0.012	0.008	0.003	0.005	0.004
Th^{4+}		0.007	0.038	0.039	0.018	0.038	0.040	0.039	0.158	b.d.l.
U^{4+}		0.001	0.004	0.005	0.006	0.002	0.002	0.000	0.000	0.000
P^{5+}		1.017	1.005	1.024	1.019	1.017	1.014	0.984	0.947	1.014
Total cations (S)		1.987	1.991	1.983	1.987	1.984	1.988	1.992	1.992	1.989
p (REEmnz)		0.976	0.927	0.867	0.874	0.906	0.911	0.943	0.721	0.994
p (cher)		0.010	0.071	0.088	0.050	0.067	0.079	0.023	0.195	0.000
p (hut)		0.001	0.002	0.005	0.006	0.013	0.009	0.033	0.081	0.005
p (xtm)		0.013	<0.001	0.040	0.070	0.013	0.003	<0.001	0.003	0.001

Note: Z1–Z9 refer to monazite zones described in text. Prefix for all samples is IV16-XX. Oxide values are wt%. Detection limit (d.l.) quoted at 99% confidence level. Cations calculated for 4 oxygens. p (REEmnz) = proportion of monazite end-member ($\sum$REE), p (cher) = proportion of cheralite end-member (1-([$\sum$REE + Y + Si]), p (hut) = proportion of huttonite end-member (Si^{4+}), p (xtm) = proportion of YPO4 end-member in monazite (Y^{3+}). B.d.l., below detection limit.

anti-correlated trends (ΣLREE = La + Ce + Pr + Nd + Sm). The lowest ΣLREE concentrations (0.7–0.8 APFU) occur in Z8, corresponding to proportional increases in Th, Ca and to a lesser extent Si.

In all compositional plots (Figure 8b), Z8 is significantly distinct from other zones; this monazite zone has high Th and Ca and low ΣLREE (Table 5, Figure 9a), indicating that grains from this zone have significantly higher fractions of huttonite [ThSiO4] and cheralite [$Ca_{1/2}Th_{1/2}PO4$] end-members than all other monazite zones. Zones 8 and 9 have been defined such that analyses with Th^{4+}_mnz > 0.02 APFU are Z8, and <0.02 APFU are Z9. In actuality, Z8 and Z9 analyses are fairly evenly spread from the highest Th^{4+}_mnz (~ 0.19

TABLE 5 Summary of monazite compositional zones and microstructural locations

Zone	Samples	Location	Th^{4+} APFU	*p (REEmnz)*	*p (cher)*	*p (hut)*	*p (xtm)*	*n*
Z1	03A, 08	c, m	0.0003–0.0153	0.956–0.981	0.001–0.029	0.006–0.018	0.007–0.013	8
Z2	03A, 07, 08	c, m	0.0111–0.0566	0.890–0.954	0.036–0.105	0.006–0.022	Bdl–0.015	55
Z3	03A, 07, 08	r, m	0.0165–0.0757	0.840–0.887	0.064–0.125	0.002–0.017	0.024–0.060	139
Z4	03A	i, l	0.0181–0.0283	0.853–0.886	0.035–0.075	0.005–0.019	0.060–0.072	5
Z5	12	r, m	0.0279–0.0457	0.881–0.914	0.056–0.082	0.010–0.023	0.008–0.029	22
Z6	12, 16	c, r, m	0.0238–0.0577	0.858–0.968	0.010–0.113	0.007–0.035	Bdl–0.025	85
Z7	16	r*, m	0.0192–0.0591	0.913–0.960	0.003–0.054	0.012–0.055	Bdl–0.001	15
Z8	22A, 22B	i, g, m	0.0621–0.1879	0.681–0.861	0.111–0.227	0.024–0.091	0.002–0.004	10
Z9	22A, 22B	i, m	Bdl–0.0141	0.946–0.994	Bdl–0.038	0.003–0.042	Bdl–0.013	73

Note: Z1–Z9 are monazite zones defined in text. The chemistry of zones is summarized in Figures 7 and 8. Prefix for all samples is IV16-XX; c, core; r, rim; r*, rims (discontinuous); m, matrix; i, isolated grains; l, leucosome; g, garnet inclusion; bdl; below detection limit. p (REEmnz) = proportion of monazite end-member (∑REE), p (cher) = proportion of cheralite end-member (1-([∑REE + Y + Si]), p (hut) = proportion of huttonite end-member (Si^{4+}), p (xtm) = proportion of YPO4 end-member in monazite (Y^{3+}). *n* = number of monazite grains. Detection limits: Th^{4+} = 0.0003 APFU; *p (REEmnz)* = 0.0045; *p (cher)* = 0.0004; *p (hut)* = 0.0008; *p (xtm)* = 0.008.

APFU; Z8) to the lowest (<0.0003 APFU; Z9, Figure 8), but with a distinct data gap in Th^{4+}_mnz between 0.014 APFU and 0.062 APFU (Table 3). Z9 has very low Th, with only 11 of 57 analyses above the detection limit. The difference between grains that preserve high rather than low Th compositions in the two UHT samples is a combination of grain size and microstructural location. Larger grains and those included in garnet preserve higher Th compositions than smaller grains located interstitially.

The Th/U ratio in monazite is relatively constant in amphibolite facies zones (Z1–Z4) and granulite facies Z5 (means of 4.3–11.3, Figure 8c). Th/U then increases from Z6 to Z8 (means of 42, 64 and 531 for Z6, Z7 and Z8, respectively). Of the Z9 analyses with Th above the detection limit, Th/U ratios are variable but the lowest in the sequence (0.5–24.3, Figure 8c).

6.4 | Monazite U–Pb geochronology

The different chemical zones identified by EPMA mapping were targeted (size permitting) for U–Pb geochronology. All samples in the study have complex spectra of Pb-corrected $^{206}Pb/^{238}U$ dates, with a total spread between 347 ± 20 and 154 ± 16 Ma, (Figure 10 and Appendix S3). Date ranges for all amphibolite and granulite facies monazite zones (Z1–Z7) overlap and mostly fall in the interval 320–240 Ma. Analyses on monazite from the UHT samples are fewer due to these monazite grains being small and yield more scattered dates in the range circa 300–150 Ma (Z8 and Z9). There is no systematic age difference between grains in different microstructural locations either within or between samples. Additionally, the range of dates for all monazite zones overlap, and for the zones that yield a significant number of analyses (Z2, Z3, Z4, Z5 and Z6) the main cluster is between 275 and 290 Ma. 'Main clusters' (Figure 10c) were defined on statistically homogenous populations (e.g., Spencer et al., 2016). Data was filtered by removing the smallest number of analyses possible to produce and MSWD <2, with the most outlying data removed first. The main cluster for Z2 is 290 ± 2.5 Ma, for Z3 is 280 ± 2.5 Ma, for Z4 is 279 ± 6.9 Ma, for Z5 is 276 ± 6.7 Ma and for Z6 is 275 ± 2.9 Ma. Notably, the youngest, although scattered, dates to 150 Ma are all from Z9 monazite in UHT samples. The overall data show two major age peaks at 290 ± 1.7 Ma and 271 ± 1.7 Ma and one minor peak at 173 ± 16 Ma (Figure 10).

7 | DISCUSSION

7.1 | Whole rock Th budget

The extensive data set of Th concentrations acquired with the two methods (XRF and GRS, Figure 3; Alessio et al., 2018) show that Th is retained in the metapelitic rocks up to the highest grade of regional metamorphism (~900°C; Redler et al., 2012), consistent with the findings of Schnetger (1994), Bea and Montero (1999) and Bea (2012). The retention of whole rock (WR) Th during pre-peak to peak metamorphism of pelites to granulite facies conditions is consistent with the trends found in several other terranes worldwide (e.g., Alessio et al., 2018; Andreoli et al., 2006; Horton et al., 2016; Skrzypek et al., 2018; Williams et al., 2018).

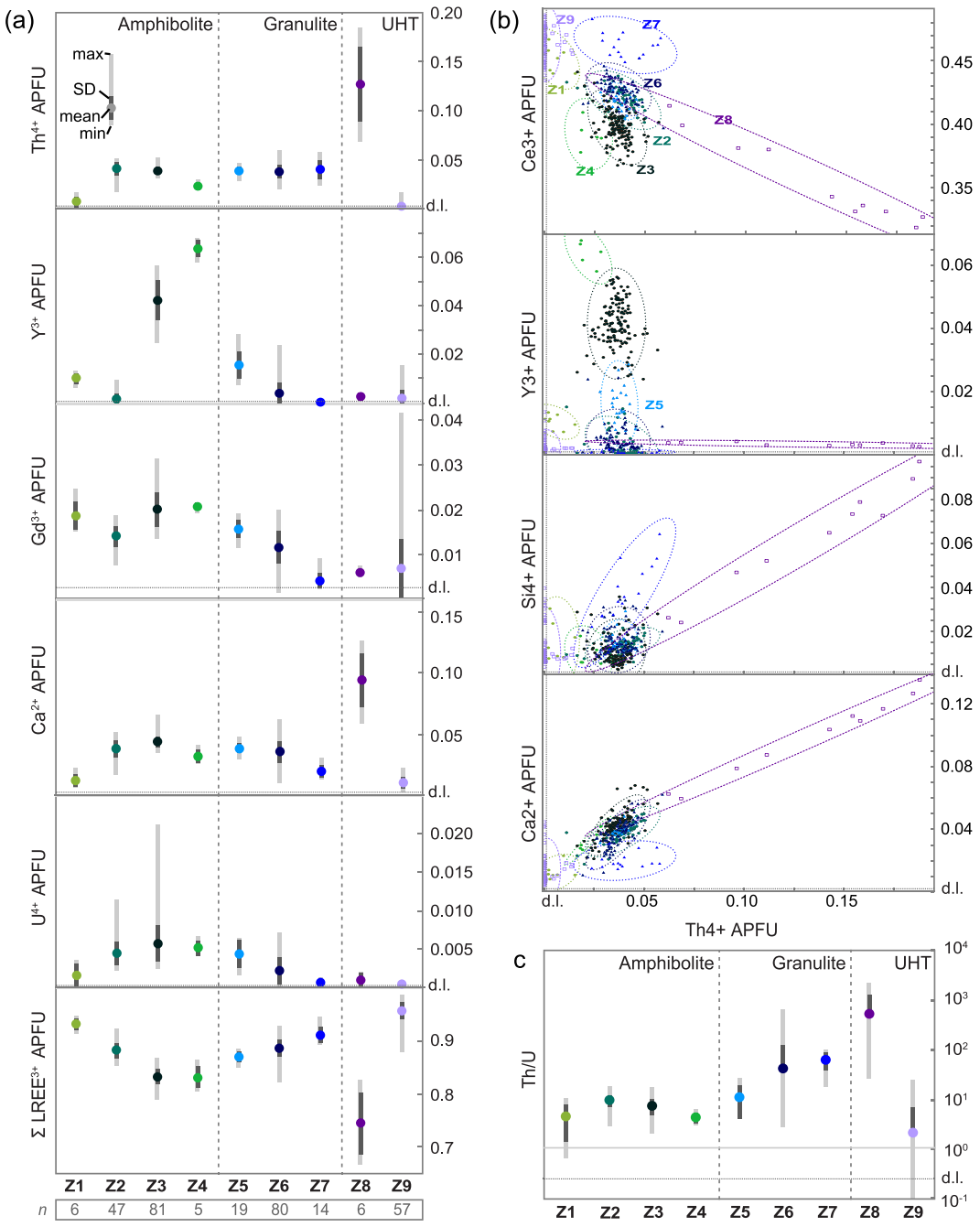

FIGURE 8 Harker and boxplots of EPMA point analyses of monazite from zones 1–9 (labelled Z1–Z9 respectively). Z1–Z4 occur in amphibolite facies samples, Z5–Z7 in granulite facies samples and Z8–Z9 in UHT samples. Number of analyses for each zone are given at the base of part (a). (a) Boxplots of chemical compositions of monazite (atoms per formula unit, APFU, normalized to 4 oxygen atoms) from zones Z1–Z9. Boxplots show dispersion of data, the interquartile range (IQR; Q1, quartile 1, Q3, quartile 3) and median values for each element. Dotted lines indicate metamorphic facies changes within the sequence. (b) Harker plots of monazite EPMA point analyses showing the range of compositions within each monazite zone, and the overlap between zones. Mahalanobis ellipses show range of compositions for each monazite zone (2σ). (c) Boxplots of Th/U ratios of monazite for compositional zones Z1–Z9. Boxplots show dispersion of data, the interquartile range (IQR) and median values for each element (as in (a)). Dotted lines indicate facies changes of the host rock. Note logarithmic scale [Colour figure can be viewed at wileyonlinelibrary.com]

By contrast, the UHT samples have significantly lower Th content than other samples in this study. This observation is in agreement with the whole rock geochemistry data of Ewing et al. (2014), which show a decrease in WR Th concentration in the septa of an order of magnitude with respect to amphibolite and granulite facies samples. As this depletion of WR Th is only observed in the UHT septa and the monazite in these

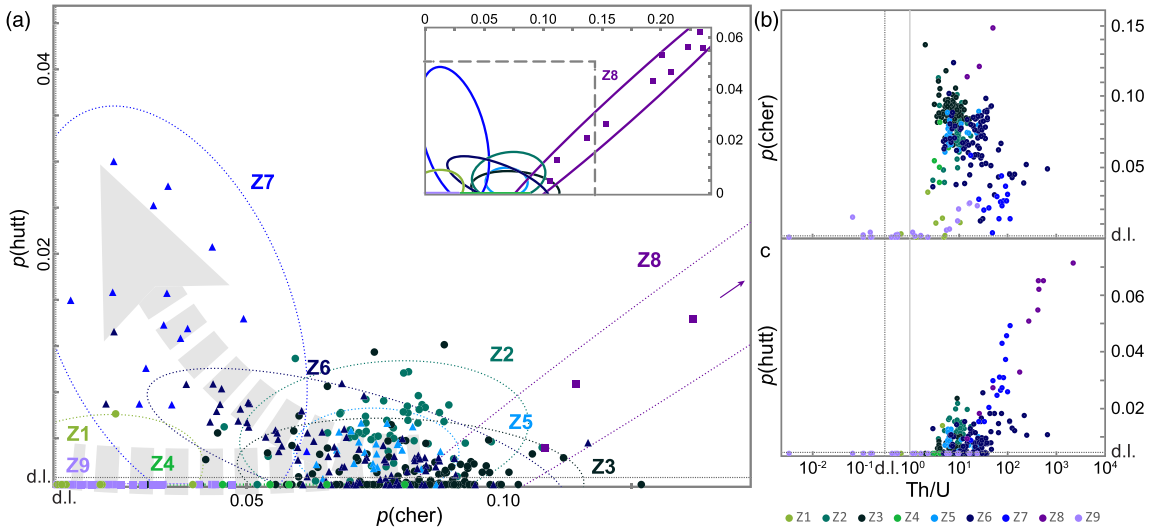

FIGURE 9 Fractions of Th-end-members of monazite cast from EPMA point data and normalized to p (cher) + p (hutt) + p (mnz) = 1, the proportions of the cheralite (Th–ca–P), huttonite (Th–Si) and Y + REE monazite respectively. Z1–Z9 refer to monazite zones Z1–Z9 described in text. (a) Relative proportion of Th-end-members cheralite and huttonite. Mahalanobis ellipses show range of compositions for each monazite zone (2σ). Dashed arrow represents interpreted changes to the cheralite/huttonite ratio with metamorphic grade. (b) Proportion of cheralite versus Th/U ratio. (c) Proportion of huttonite versus Th/U ratio [Colour figure can be viewed at wileyonlinelibrary.com]

samples has small grain size and low volume proportion (mode), the process that causes the efficient extraction of Th from the residual rocks must only occur at very high crustal temperatures (i.e., > ~900°C) or in samples with chemistry similar to the UHT granulites in this study. In agreement with previous studies of UHT samples (Ewing et al., 2014; Stepanov et al., 2014) and modelling (Yakymchuk et al., 2018; Yakymchuk & Brown, 2014), we interpret metamorphism to UHT conditions at Ivrea to have involved significant dissolution of monazite into (extracted) melts, and that the solubility of monazite was most advanced in the UHT metapelitic septa. The presence of monazite in the UHT rocks (Figure 10; Ewing et al., 2013) could suggest either that the temperature for total monazite dissolution is higher than previously reported (at least in the rocks we have studied; e.g., Kelsey et al., 2008; Spear & Pyle, 2010; Yakymchuk & Brown, 2019) and/or that monazite dissolution was kinetically or physically inhibited (see Yakymchuk & Brown, 2019). The low volume proportion of monazite, marked decrease in average grain size and the location of monazite primarily at grain boundaries within the matrix of the two UHT samples (Table 3 and Figures 6, 7), supports that significant monazite dissolution has occurred at UHT conditions. This monazite dissolution may have been further facilitated by interaction with mafic melt surrounding the septa as the UHT samples have higher CaO than other pelite samples in this study.

Th_WR ppm concentrations of samples collected from the same outcrops as Th_GRS measurements broadly lie within the spread of Th_GRS data (Figure 3; Alessio et al., 2018). Values from XRF analyses that fall outside the spread of GRS data from the same outcrops most likely reflect the decimetre to metre scale of heterogeneous layering, and the variable proportion of mafic and calc–silicate rocks in the sequence that contribute to the GRS outcrop-scale data.

7.2 | Monazite stability

Monazite is present in all samples in this study. This is in contrast to a previous study (Guergouz et al., 2018) which found no monazite in the studied granulite facies rocks in the IVZ. This indicates that in certain bulk rock compositions (low Ca), monazite was stable to the peak of regional metamorphism (~9.5 kbar, 900°C; Redler et al., 2012; Kunz et al., 2018). At face value, the proportion of preserved monazite measured in the samples reaches a peak in the amphibolite facies and decreases through the granulite facies. However, the role of allanite has to be considered. Allanite volume proportion in the granulite facies samples (IV16-12 and IV16-16) is non-negligible (Figure 6) and allanite in these samples is predominantly hosted in allanite–Th-orthosilicate aggregates on monazite grain boundaries. These aggregates were interpreted by Bea and Montero (1999) to be products of the retrograde breakdown of monazite. Some of the apatite in these samples is also likely retrograde in origin (Appendix S4; Bea & Montero, 1999). This indicates that

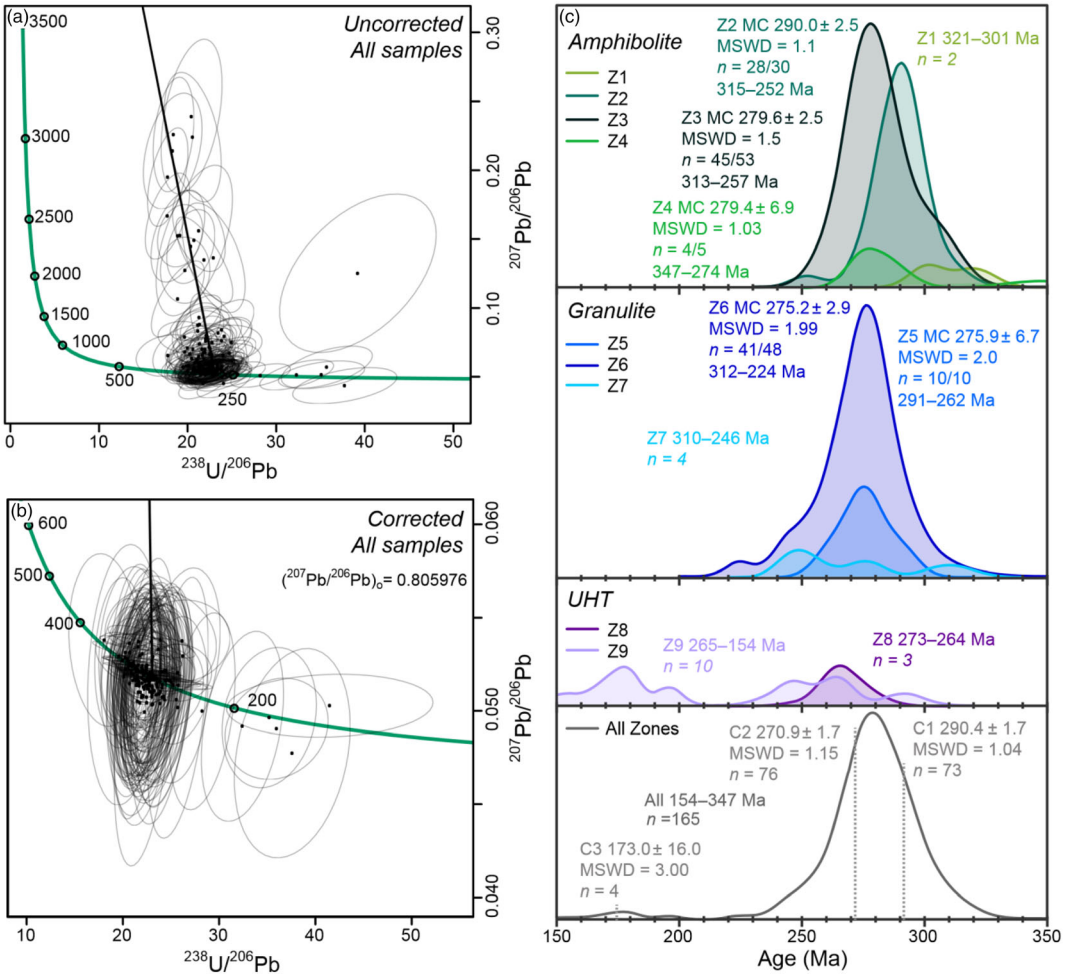

FIGURE 10 LA–ICP–MS monazite geochronology from the Ivrea–Verbano zone. (a) Tera–Wasserburg plot of uncorrected monazite data; (b) Tera–Wasserburg plot of 207Pb-corrected monazite data. Bold black line in parts (a) and (b) is the regression line for the initial $^{207}Pb/^{206}Pb$ ratio ($^{207}Pb/^{206}Pb_0$) used in the 207 Pb correction; (c) probability density plot of LA–ICP–MS monazite Pb corrected $^{206}Pb/^{238}U$ dates. Ranges of $^{206}Pb/^{238}U$ ages are shown for all zones and weighted average $^{206}Pb/^{238}U$ ages are shown for compositional zones Z2, Z3, Z4, Z5 and Z6. Statistically meaningful ages could not be calculated for Z1, Z7, Z8 and Z9. In each legend the samples are listed in order of increasing metamorphic grade. Pb correction was performed using 207 method. MC, main cluster; C1–3, Cluster 1–3 determined by radial plot [Colour figure can be viewed at wileyonlinelibrary.com]

proportion of monazite in samples IV16-12 and IV16-16 were higher at the peak of metamorphism. Therefore, the observed decrease in monazite proportion from amphibolite to granulite facies samples is not indicative of monazite dissolution into melt, but rather subsolidus retrogression. It is unclear whether a similar process occurred in the UHT samples as monazite and allanite occur as isolated grains. Other studies have reported an increase in monazite volume proportion (and grain size) with metamorphic grade (e.g., Foster et al., 2002; Franz et al., 1996; Rubatto et al., 2001; Schulz, 2017; Skrzypek et al., 2018; Williams, 2001; Williams et al., 2018). We contend that such a trend may also have been present in the IVZ, but the retrograde reactions in the rock partially obscure the record.

The maximum grain size of monazite increases with metamorphic grade (Figure 6, Table 3); however, as large(r) monazite grains are few in each sample they do not greatly affect the sample average grain size (e.g., Nemchin et al., 2001). The maximum grain size increase may be the result of processes which favour the growth of large grains of monazite, such as the REE-saturated melt infiltration model proposed by Yakymchuk and Brown (2019), decompression melting (e.g., Johnson et al., 2015), or Ostwald ripening (dissolution of smaller grains and precipitation onto larger grains; e.g., Nemchin et al., 2001). However, all these mechanisms would typically preserve lower temperature cores, which are not observed in the granulite facies samples and so cannot explain the full range of textures observed here.

7.3 | Monazite chemistry and mechanisms of formation

The monazite geochronology presented in Figure 10 shows that all monazite in the investigated samples is metamorphic and records a protracted growth (and dissolution) history (see Section 7.5). Monazite zones Z1–Z3 and Z5–Z8 preserve a temporal series of chemical zones (Figure 11), the compositions and order of which are consistent with the recorded and modelled progression of major and accessory mineral growth along the metamorphic field gradient in the IVZ (Figure 6; Redler et al., 2012). Zones Z4 and Z9 are interpreted to have formed on the retrograde path (see below) and thus are not part of the pre-peak to peak sequence of monazite formation. On the basis of the investigation of monazite composition presented herein, we contend that retrograde or cooling related monazite makes up only a small proportion of the total monazite in the IVZ metapelites (only the volumetrically minor zones Z4 and Z9).

High LREE Z1 monazite is found in the cores of grains, only in amphibolite facies samples IV16-03A and IV16–08. Similar patchy core textures have been reported from other terranes (Skrzypek et al., 2018; Williams et al., 2018). In both of these published examples, the high LREE zones can be traced through metamorphic grade changes, originating as aggregates of small monazite grains in lower-amphibolite facies rock, pseudomorphed after (probable) allanite (Skrzypek et al., 2018; Williams et al., 2018).

The transition between Z1 and Z2 monazite, characterized by a change to higher Th and lower REEs, indicates the progressive incorporation of Th, predominantly via the cheralite substitution, within monazite at inferred lower-to-mid amphibolite facies conditions. We interpret this as a continuation of the allanite-consuming reaction

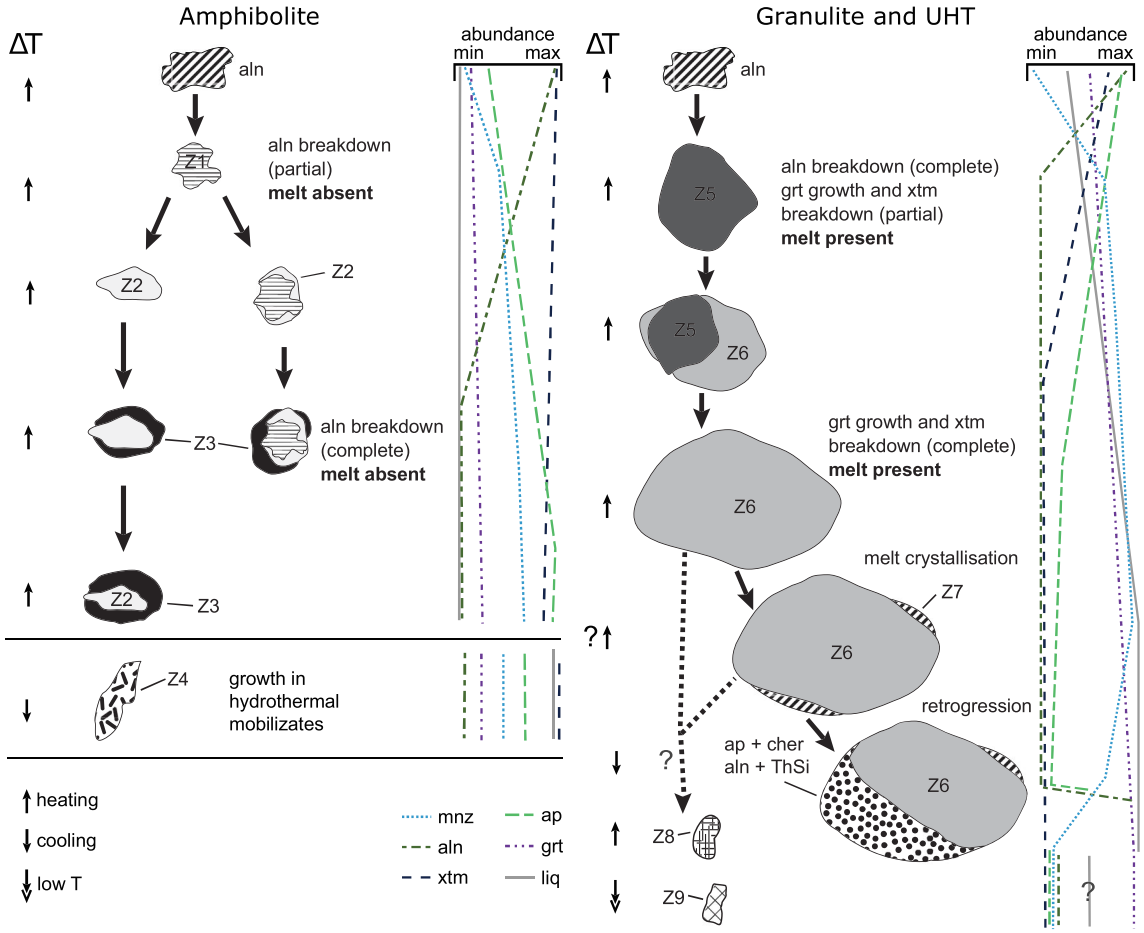

FIGURE 11 Interpretative monazite formation summary from the IVZ. Z1–Z9 are monazite zones described in text. Schematic abundance plot shows changes in mineral and melt abundance relative to the growth of monazite zones. Refer to Figure 6 for absolute volume proportions of minerals. Dashed line indicates uncertainty of genetic relationship between granulite facies and UHT monazite. Melt abundance from Redler et al. (2013). Ap, apatite; aln, allanite; grt, garnet; liq, melt; mnz, monazite; xtm, xenotime [Colour figure can be viewed at wileyonlinelibrary.com]

that forms Z1 monazite. We propose that as the continuous allanite breakdown reaction progresses to higher temperature, monazite accommodates more Th that is released from high (er)-Th allanite (see also Skrzypek et al., 2018), primarily via the cheralite coupled substitution mechanism.

Zone 3 monazite is characterized by a higher Y content than Z1–Z2 and likely formed in a xenotime-bearing (i.e., Y buffered) assemblage (as there is xenotime in amphibolite facies samples), as such assemblages correspond with high Y monazite (e.g., Pyle & Spear, 2003). On the basis of previous studies of garnet, monazite and xenotime, Y-in-monazite increases with temperature (e.g., Hacker et al., 2019; Heinrich et al., 1997; Pyle & Spear, 2003) indicating that all subsolidus monazite (Z1, Z2 and Z3) in the IVZ is grown during up temperature metamorphism.

Lower grade (Z1–Z3) monazite has reasonably variable compositions whereas granulite facies monazite has a smaller range of compositions (Figure 8), showing that the granulite facies grains are more chemically equilibrated. This is in line with results from other terranes which showed that (effective) chemical equilibrium for Th and LREE was reached by ~600°C (Skrzypek et al., 2018; Williams et al., 2018). At temperatures below 600°C, variable monazite compositions and Th/U ratios likely reflect variable local availability of Th due to the grain size and composition of prograde allanite (which breaks down to form monazite).

Zone 4 monazite occurs only in muscovite-rich leucocratic veins in the lowest grade sample studied, IV16-03A. These leucocratic veins were interpreted by Bea and Montero (1999) to have been hydrothermal mobilizates, rather than partial melts. For this reason we do not consider Z4 monazite as part of the pre-peak monazite reaction sequence, but rather formed during the retrograde evolution.

It is possible to infer that garnet mode was either increasing or remaining unchanged during the formation of zones Z5, Z6 and Z7, on the basis of the relatively low concentration of Y and Gd (which have a strong affinity for garnet) in these zones. This is consistent with a *P–T* path involving heating and pressure increase. In this scenario, the reactive bulk composition becomes undersaturated in Y due to disappearance of xenotime and the Y available to monazite decreases (e.g., Pyle et al., 2001). As a consequence, Z5–Z7 monazite formed at granulite facies is depleted in Y and HREE compared with the last amphibolite facies monazite, Z3, which grew in the presence of xenotime and lower volume proportion of garnet. We can exclude that zircon is the source of HREE as the mode of zircon is constant across the sequence (Figure 6). Large monazite grains in sample IV16–16 containing Z6 and Z7 occur predominantly within or adjacent to leucocratic layers (Figure 5), suggesting that these monazite grew in the presence of silicate melt (see also Bea & Montero, 1999). The higher Th/U ratio of Z7 relative to Z6 suggests that it formed at the peak of metamorphism rather than on the retrograde path (e.g., Yakymchuk & Brown, 2019; Yakymchuk et al., 2018).

Compositions for zones Z2 and Z6 are similar, but Z6 has significantly higher Th/U ratios and Z6 monazite occurs as rims on Z5 monazite in IV16-12. Therefore, these two zones cannot be equivalent as monazite Z5 does not occur in the amphibolite facies samples. The granulite facies zones show a decreasing trend in Y and Gd with grade but have similar Th concentrations (Figure 8). This confirms that Y-in-monazite and Th-in-monazite are controlled by two different processes, the former by xenotime and garnet (e.g., Pyle et al., 2001) and the latter most likely by silicate melt and temperature (Stepanov et al., 2012; Yakymchuk et al., 2018).

The lack of amphibolite facies cores in the granulite facies samples is not observed in recent studies of progressive metamorphism in lower-pressure rocks (e.g., Skrzypek et al., 2018; Williams et al., 2018). One explanation is that earlier generations of monazite were fully consumed by processes such as dissolution–precipitation creep (e.g., Wawrzenitz et al., 2012), facilitated by elevated strain and the presence of melt in the granulite facies samples. However, this would present a contradiction when considering melt extraction as suggested by Redler et al. (2013). Melt loss is commonly thought to be a mechanism by which REE and Th are extracted from the crust. If monazite was the REE- and Th-host before melting and recrystalised in the presence of melt, then some monazite components would likely be extracted with the melt. An alternative which may better explain the observations from the granulite facies samples is that allanite was the REE and Th host prior to or during initial and early melting of these rocks. The slope of allanite-to-monazite reaction is positive (Spear, 2010; Williams, 2019) and as such the stability of allanite expands to higher temperature with increasing crustal depth. The thermal gradient reported by Redler et al. (2012) presents the possibility that in deeper, higher-temperature rocks at Ivrea, monazite did not appear until close to, at or above the solidus (Figure 12). The stability of allanite to solidus or suprasolidus conditions at higher pressures may help explain the absence of cores of amphibolite facies monazite in the granulite facies rocks, in contrast to the record in lower pressure terranes (e.g., Skrzypek et al., 2018; Williams et al., 2018), and would imply that the growth of granulite facies Z5, Z6 and Z7 only occurs once terminal allanite stability has

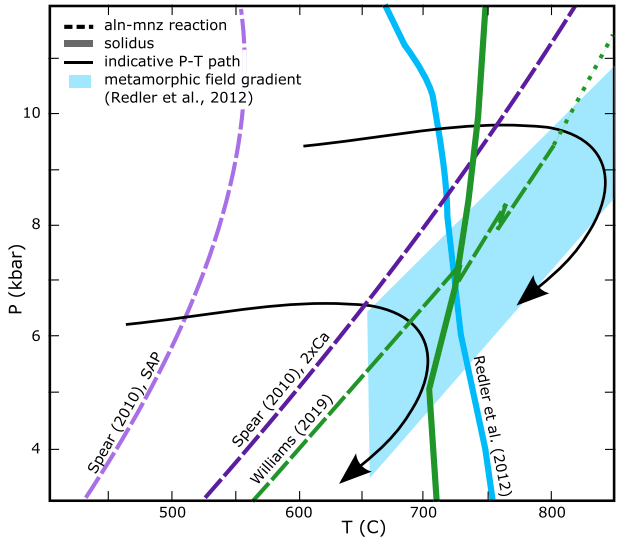

FIGURE 12 Schematic P–T diagram showing the relationship between allanite, monazite and melt from published examples. At high pressures, allanite may persist above the solidus, with no prograde monazite produced (e.g., Williams, 2019). Allanite-monazite reaction boundaries from Spear (2010) (SAP and 2xCa) and Williams (2019) (sample IV16-07) showing the positive slope of the reaction. Solidus from Redler et al. (2012) (sample IZ 140) and Williams (2019) (sample IV16-07), both unmelted amphibolite facies samples. Indicative P–T paths for amphibolite and granulite facies samples after Redler et al. (2012). SAP, Shaw's average pelite (Shaw, 1956); 2xCa, Shaw's average pelite with Ca value doubled (Spear, 2010) [Colour figure can be viewed at wileyonlinelibrary.com]

been exceeded. In this scenario, it is inferred that LREE for monazite growth in granulite facies rocks came from allanite and P from apatite and xenotime (Figure 6). Whereas whole rock P_2O_5 has a major influence on apatite volume proportion, more subtle variation can be attributed to changes in the relative stability of the phosphate mineral species with metamorphic grade.

In contrast to the evidence from natural samples, forward thermodynamic models (Kelsey et al., 2008; Spear & Pyle, 2010; Yakymchuk, 2017) are unable to account for progressive, up temperature growth of monazite (nor zircon) above the solidus as the components that comprise monazite are not regarded as being present in high enough concentrations in major minerals to allow growth of monazite by major mineral breakdown. Rather, silicate melt is the only major phase that has appreciable concentrations of monazite- (and zircon-)forming components. As the volume proportion of melt increases with increasing temperature, equilibrium models predict that monazite mode progressively decreases. Studies based on natural samples have suggested an Ostwald ripening mechanism (e.g., Nemchin et al., 2001; Rubatto et al., 2001; Vavra et al., 1996; Williams, 2001) could occur at anatectic conditions. However, these processes are not grounded in equilibrium thermodynamics and thus cannot be modelled as part of the typical calculated pseudosection approach of modern metamorphic studies. As such, explaining prograde suprasolidus growth of monazite (and zircon) remains an issue, particularly in sequences where allanite is not present. Although the mechanism of Ostwald ripening is consistent with observations from amphibolite facies monazite, it cannot explain the lack of amphibolite facies zones in cores of granulite facies monazite. Therefore, other processes (e.g., dissolution–precipitation creep; Wawrzenitz et al., 2012) or the later appearance of monazite due to the positive slope of the allanite-to-monazite reaction may be responsible for at least part of the monazite record here.

Recently, Yakymchuk and Brown (2019) suggested that prograde suprasolidus accessory mineral growth could occur via infiltration of melt generated at deeper crustal levels into shallower anatectic crustal rocks. By this logic, hotter melts generated at deeper crustal levels have higher LREE, Th and Zr concentrations than shallower melts due to more advanced dissolution of the accessory minerals, which when mixed together cause oversaturation of melt with respect to LREE and Th (and Zr), leading to (prograde) monazite precipitation on existing grains. The highest grade rocks in Val Strona (sample IV16–16 in the present case) are closely (~2 km) underlain by metabasic granulites of the Mafic Complex, meaning that only a thin pelitic section exists in between IV16-16 and the Mafic Complex in which melts with more LREE and Th could be generated. Although we do not discount this possibility, the systematic trends in Th and trace element behaviour that we document suggests that open system behaviour pertaining to the trace elements was not the major controlling factor, at least for the non-UHT samples.

The UHT samples have a distinct monazite population in composition, texture, mode and partially age and contain no remnants of monazite zones observed in the lower T granulite samples of the regional sequence. In the UHT samples monazite volume proportion is very low (0.001–0.0045 vol.%) and monazite compositions show a range between high (Z8) and low Th (Z9). The high Th content in monazite at UHT can be explained by a high DThmnz/liq (e.g., Stepanov et al., 2012) in samples with a low monazite volume proportion that have undergone significant partial melting and melt extraction. The range in compositions between Z8 and Z9 is interpreted to indicate that Z9 monazite was formed from Z8 monazite, with some Z8 grains retaining a partial record of this process. The very low monazite Y content is consistent with a high mode of garnet in

the UHT samples. Although monazite, apatite and allanite abundance are low, and the sum of the three is less than for lower grade samples, the UHT samples have similar LREE contents to other samples in this study. The reason for this disparity between apparent whole-rock LREE retention and Th loss in the UHT samples is not possible to definitively discern, but must mean that another phase also hosts LREE. The most likely candidate is feldspar. The UHT samples contain a high volume proportion of feldspar (40–50%) and garnet (20–25%), and much of the feldspar occurs in leucosomes, indicating that it was a product of the melting reactions. Interaction between the metapelite residuum and tonalitic melt may have enhanced the production of plagioclase and therefore the sequestration of REE in the UHT samples. LREE concentration data for feldspars in the UHT septa are not available. However Ce values for feldspar in the Val Strona section are 1.86–111 ppm (plagioclase) and 0.61–3.99 ppm (K-feldspar; Bea & Montero, 1999). Given the high volume proportion of feldspars in the samples, and by assuming the above LREE concentrations are retained in higher-temperature feldspars, Ce values in the range 50–100 ppm in UHT feldspar would be sufficient to account for the Ce concentrations in the UHT rocks, with a small contribution from garnet. High LREE compositions, typical of low temperature monazite (e.g., Allaz et al., 2013; Cabella et al., 2001; Rasmussen & Muhling, 2007) and recorded by Z9 monazite, could be the result of episodic formation of monazite on the retrograde path, for example, during late fluid circulation in the Mafic Complex (Vavra & Schaltegger, 1999).

Given the high bulk Ca in the UHT samples relative to other pelites in this study (Table 2) and their location within the mafic complex, it is possible that the UHT granulite samples were contaminated by tonalitic melt. Despite the lower stability of monazite in Ca-rich rocks (e.g., Spear, 2010; Stepanov et al., 2012), this apparent change in rock chemistry did not result in complete dissolution of monazite in the septa. The presence of monazite with high Th contents in the UHT septa shows that monazite can in some cases resist high temperature dissolution processes.

7.4 | Changes to monazite Th end-member fractions with metamorphic grade

The fractions of the two Th-end-members of monazite, cheralite and huttonite, change with metamorphic grade in the IVZ (Figure 9a). Amphibolite facies monazite zones (Z1–Z3) favour cheralite rather than huttonite in terms of Th. This is consistent with other studies of monazite chemistry over metamorphic grade changes (Skrzypek et al., 2018; Williams et al., 2018). Above the solidus, monazite increasingly favours huttonite at the expense of cheralite which is particularly evident from Z5 to Z6, a trend which is also reported by Skrzypek et al. (2018) in the Ryoke Belt. We interpret this as the probable result of one or more of (a) unfavourable thermodynamic properties of huttonite to allow its presence in significant proportion at subsolidus temperatures and pressures (e.g., Mazeina et al., 2005; Robie & Hemingway, 1995); (b) cheralite being more soluble in melt than huttonite, as silicate melt produced from melting of metapelites is typically saturated in Si but not Ca; and (c) buffering of P (and possibly Ca) in monazite by the presence of apatite in amphibolite facies samples, with apatite volume proportion decreasing by dissolution into melt through the granulite facies (Figure 6). The preference for higher huttonite (Si) fractions in monazite with increasing temperature could provide an important mechanism by which monazite remains stable to extremely high temperatures (>900°C, cf. Yakymchuk, 2017) as the stability of the huttonite component of monazite does not require P or Ca saturation.

Monazite grains in the UHT rocks show a different Th solid-solution trend to the granulite facies samples, having huttonite-rich compositions which also have a high proportion of cheralite (Z8; Figure 9a inset), as well as a population with low fractions of cheralite and near zero huttonite (Z9; Figure 9a). Zone Z8 is enriched in both cheralite and huttonite due to melt-driven enrichment in total Th (see above).

There is also a marked increase in the Th/U ratio of monazite from the lower granulite facies (Z5) to the UHT conditions (Z8; Figure 8). This is consistent with previous findings from the IVZ (Bea & Montero, 1999) and also more generally (Rubatto et al., 2006; Taylor et al., 2014, 2016; Yakymchuk et al., 2018), in that monazite has a stronger preference for Th over U with increasing temperature. The increase in Th/U above the solidus is not correlated with the fraction of cheralite (p [cher]; Figure 9b), but is correlated with the increase in huttonite fraction (p [hutt], Figure 9c), showing that huttonite has a stronger influence on controlling Th/U in monazite, at least in melt-bearing rocks. A similar positive correlation between huttonite fraction and Th/U in monazite was observed at Mt Stafford (Williams et al., 2018).

7.5 | Monazite ages

The purpose of collecting age data in the context of this study is primarily to decipher whether monazite is metamorphic or detrital. Overall our monazite data conform with the range and complexity of zircon and monazite ages reported in previous studies and attributed to

metamorphism (e.g., Ewing et al., 2013; Guergouz et al., 2018; Kunz et al., 2018; Vavra et al., 1999).

Figure 10a shows a clear discordant trend in the U–Pb unknown data across all samples in this study. This trend is attributed to common Pb and applying the ^{207}Pb correction (Figure 10b, see Appendix S2 for details) produces age distributions with less scatter and slightly younger ages (c. 5 Ma). In addition to the common Pb trend, there is a spread in the ^{206}Pb/^{238}U ratios which is typically attributed as either Pb loss during retrogression or protracted growth of monazite (e.g., Gasser et al., 2015; Kirkland et al., 2016; Rubatto et al., 2001). The progression of monazite chemical zones identified in this study would suggest that this scatter has some geological significance. The same conclusion was reached by Guergouz et al. (2018) and Peressini et al. (2007) in reference to similar distributions of monazite and zircon dates from the metapelites of the IVZ and Mafic Complex, respectively. If Pb loss has affected the data it must have occurred within the period of high temperature metamorphism as there is no other Pb loss trend observed in the data (Appendix S2).

Monazite in the cores of amphibolite facies grains, Z1, yields the oldest dates (321 ± 16.6 and 301 ± 14.4 Ma; both from IV16-03A). The lack of a clear and distinct age peak relating to the Variscan regional metamorphism (c. 320–300 Ma; Ewing et al., 2013; Kunz et al., 2018; Vavra et al., 1999) likely reflects the fact that the moderate *P*, moderate *T* conditions of the Variscan regional metamorphism (Ewing et al., 2013; Kunz et al., 2018; Vavra et al., 1999) were generally not conducive to the formation of monazite (i.e., were within the allanite stability field; Spear, 2010).

Ages from Z3, Z4, Z5 and Z6 monazite from the Val Strona samples (280 ± 2.5, 279 ± 6.9, 276 ± 6.7 and 275 ± 2.9 Ma, respectively; Figure 10c) are in agreement with previously reported monazite ages (283 ± 6 and 279 ± 6 Ma; Guergouz et al., 2018) from the same sequence and with zircon ages from amphibolite facies rocks in Val Strona (280 ± 2 and 272 ± 1 Ma; Kunz et al., 2018). All these published age constraints are interpreted as dating metamorphism and partial melting in the metapelites and are within uncertainty of or shortly postdate the circa 292–282 Ma intrusion of the upper Mafic Complex (Peressini et al., 2007). The texturally older monazite zone (Z2) that could be dated with confidence records an age of 290 ± 2.5 Ma which is within the range of the published zircon age spectra but has not been clearly identified in monazite before. In the UHT samples, larger monazite grains (>50 μm Ø) and those included in garnet (Z8) yield scattered dates in the range 273–264 Ma, whereas smaller grains (<50 μm Ø) located interstitially (Z9) yield scattered dates in the range 265–154 Ma. The young dates, although scattering in the range 181–154 Ma ($n = 4$), are unique to the UHT samples, and in particular to Z9 monazite.

Our age data are consistent with chemical evidence that monazite in the IVZ predominantly records the pre-peak and peak (Permian) history of the terrane. We conclude that the samples contain no detrital monazite and that all the monazite investigated formed during metamorphism. Further dissection of the geological significance of dates from individual monazite zones is treated with caution as the timescale of metamorphism is similar to the uncertainty associated with the LA–ICP–MS ages obtained.

7.6 | Differentiation of continental crust through partial melting

The IVZ lower crustal section contains abundant mafic and calc-silicate rocks throughout (e.g., Bertolani, 1968; Rutter et al., 2007) and the voluminous Mafic Complex is located at the base of the section (e.g., Peressini et al., 2007; Quick et al., 2003; Sinigoi et al., 1994). The monazite record reported here supports the idea that the Mafic Complex was a major heat source and that it was emplaced at or near the peak of metamorphism. The total volume of metabasic crust in the Val Strona section (excluding the Mafic Complex) is 10–30%, with a further 8–14% metacarbonate lithologies (estimated from Bertolani, 1968; Rutter et al., 2007). However, much of the Th in the section is hosted by metapelite layers (although some of the subordinate metabasic layers contain huttonite; Förster & Harlov, 1999) that have an average Th content 70 times greater than associated subordinate metabasic layers within the pelite (metapelite layers 21.0 ± 2.5 ppm, metabasic layers 0.3 ± 0.3 ppm; from Alessio et al. (2018) and Bea and Montero (1999), respectively). These metapelitic layers comprise ~50% of the metamorphic sequence in Val Strona (Bertolani, 1968; Rutter et al., 2007). As shown here and also in Alessio et al. (2018), the process of partial melting of pelitic rock types does not result in a net loss of Th from residual rocks except in the case of extreme metamorphism, at temperatures in excess of 900°C (see also Ewing et al., 2014; Yakymchuk & Brown, 2019). This is consistent with Bea and Montero (1999) and Bea (2012) who argued that segregated melts had equal or lower Th and overall heat production than their sources, as well as observations of both Th concentrations and radiogenic heat production in numerous other metasediment-dominated terranes

(e.g., Alessio et al., 2018; Skrzypek et al., 2018; Williams et al., 2018).

The conservation of relatively high heat production (2.29 ± 0.05 μW m^{-3}; Alessio et al., 2018) in the IVZ lower crustal (granulite) metapelites may have assisted the attainment of peak temperature conditions (e.g., Jamieson et al., 1998; Yakymchuk & Brown, 2019), helped to sustain elevated thermal conditions for a prolonged (> 30 Myr; this study) period (e.g., Clark et al., 2011; Holder et al., 2018; Horton et al., 2016; Kelsey & Hand, 2015) and resulted in slow cooling of the terrane relative to the conductive geotherm (Ewing et al., 2015; Yakymchuk & Brown, 2019).

The IVZ example shows that partial melting of metasedimentary-dominated crust can conserve its thermal potential energy (in the form of heat producing elements; Figure 3, see also Alessio et al., 2018; and Yakymchuk & Brown, 2019), in contrast to foundational studies which suggested that the lower crust is depleted in heat producing elements (e.g., Rudnick & Fountain, 1995; Rudnick & Gao, 2003). According to the calculations of Hacker et al. (2011), a minimum of 27% of samples from granulite terranes and 43% of rocks from ultra-high pressure terranes are peraluminous, pelitic metasediments. This suggests that the exposed distribution of felsic and mafic rock types in the IVZ can be considered representative of the lower crust. However, estimations of the average heat production of the IVZ (Val Strona section) are significantly higher than reported heat production for both the average lower continental crust and the average continental crust as a whole (Figure 13; Bea, 2012). The marked difference in heat production between metasedimentary and other (in this case mafic) rock types suggests that even if the proportion of metasedimentary rocks in granulite terranes is minor, the heat producing element budget, and thus radiogenic thermal energy budget, is strongly determined and controlled by the residual metasedimentary rocks (e.g., Figure 13). Average lower continental crustal heat production (0.5–0.8 μWm^{-3}; Bea, 2012) can be replicated with 20–30% metapelite (2.29 μWm^{-3}; Alessio et al., 2018) and 70–80% metabasite (0.08 μWm^{-3}; Bea & Montero, 1999), with the metapelite layers contributing circa 90% of the heat production (Figure 13). This is well below the estimates for the proportion of metapelitic crust in Val Strona (52–78 vol.%; Bertolani, 1968; Rutter et al., 2007). If the lower crust is depleted in heat producing elements as proposed by Rudnick and Fountain (1995) and Rudnick and Gao (2003), it is due to processes other than crustal melting and/or the extreme dominance of rock types with low Th and U.

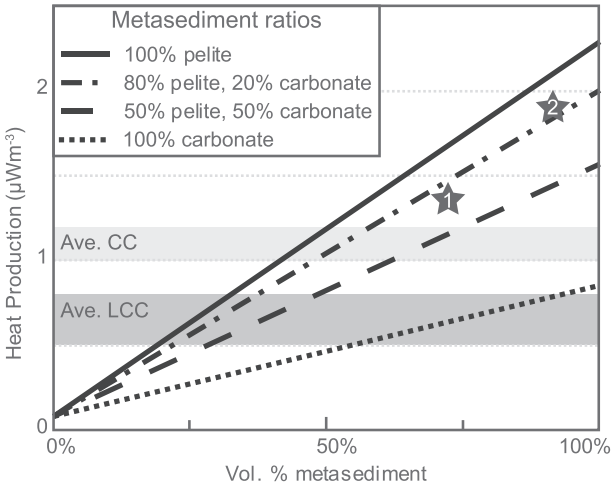

FIGURE 13 Total heat production rate for the IVZ for different ratios of rock types with different (but fixed) radiogenic heat production rates. Heat production rates for lithologies are metapelite = 2.29 μWm^{-3} (Alessio et al., 2018), metacarbonate = 0.85 μWm^{-3} (Abart et al., 2001) and metabasite = 0.08 μWm^{-3} (Bea & Montero, 1999). Stars represent IVZ heat production rates based on the proportion of pelitic, carbonate and metabasite lithologies given by (1) Bertolani (1968) and (2) Rutter et al. (2007). Oblique solid and dashed mixing lines show heat production for the terrane given different proportions of the three rock types (metapelite, metacarbonate and metabasite), from 100% metabasites at the left to 100% metasediment at the right. Heat production rate estimates for average continental crust (Ave. CC) and average lower continental crust (Ave. LCC) are shown for comparison (Bea, 2012) and are independent of vol.% metasediment calculations

8 | CONCLUSIONS

The IVZ is a tilted cross section considered to be representative of the orogenic lower crust, with pelitic rocks showing evidence for partial melting and melt extraction. Monazite in the IVZ preserves recognizable and systematic chemical composition zones that can be linked to the growth/consumption of other accessory and major minerals. The pre-peak to peak ages recorded by monazite compositional zones in the IVZ are within the range of existing zircon age data for the same section. Monazite volume proportion estimates at peak metamorphism in each sample increase to and through the granulite facies and only decrease sharply in UHT septa, showing that extreme temperatures (>900°C) or a change in the sample chemistry need to be reached before monazite is no longer present in metasedimentary granulites. On the basis of our detailed investigation of monazite we contend that allanite played a major role in the recorded monazite compositions and that monazite formed during

retrograde cooling comprises only a small proportion of the total monazite. Th contents in the lowest temperature prograde monazite are low (0.0003–0.0153 APFU), then increase to 0.0165–0.0757 APFU by the mid amphibolite facies (~650°C) and remain relatively constant to the granulite facies (~900°C, 0.0238–0.0591 APFU). Th contents of monazite grains that are large (>50 μm Ø) and included in garnet in the UHT samples are the highest in the sequence (0.0621–0.1879 APFU). These observations show that monazite is a primary control on the retention of Th in metasedimentary lower crust and indeed the deep crust. As a consequence, whole rock Th concentration is conserved from amphibolite (~650°C) to granulite facies conditions (~ 900°C), and only decreases in UHT rocks where monazite volume proportion is significantly reduced due to the approach of full monazite solubility into melt.

ACKNOWLEDGEMENTS

Mahyra Tedeschi and Arnaud Devoir are thanked for their assistance with field work. Thank you to Drs Ben Wade and Sarah Gilbert at Adelaide Microscopy for their assistance with analytical work and Stan Mertzman at Franklin and Marshall College for geochemical analysis. The authors thank Etienne Skrzypek, Simon Harley, Chris Clark and two anonymous reviewers for thorough reviews of this work which greatly improved the quality of the arguments and presentation of data. Simon Harley and Richard White are thanked for editorial handling. This work was supported by Australian Research Council grant DP160101006 awarded to DEK and DR and an Australian Government Research Training Program Scholarship awarded to MAW. MAW acknowledges the support of the GSSA.

ORCID

Megan A. Williams https://orcid.org/0000-0002-4926-2365

Daniela Rubatto https://orcid.org/0000-0002-7425-7904

REFERENCES

Abart, R., Schmud, R., & Harlov, D. (2001). Metasomatic coronas around hornblendite xenoliths in granulite facies marble, Ivrea zone, N Italy, I: Constraints on component mobility. *Contributions to Mineralogy and Petrology*, *141*(4), 473–493. https://doi.org/10.1007/s004100100255

Ahrendt, H., Hoefs, J., Strackenbrock, I., & Weber, K. (1989). A geothermal gradient of the lower crustal section of the Ivrea-Zone during Hercynian time deduced from carbon isotopes. In *Varallo conference on the lower continental crust, Varallo, Italy* (p. 17). Spec. Pub. Consiglio Nazionale delle Ricerche.

Alessio, K. L., Hand, M., Kelsey, D. E., Williams, M. A., Morrissey, L. J., & Barovich, K. (2018). Conservation of deep crustal heat production. *Geology*, *46*(4), 335–338. https://doi.org/10.1130/G39970.1

Allaz, J., Selleck, B., Williams, M. L., & Jercinovic, M. J. (2013). Microprobe analysis and dating of monazite from the Potsdam formation, New York: A progressive record of chemical reaction and fluid interaction. *American Mineralogist*, *98*(7), 1106–1119. https://doi.org/10.2138/am.2013.4304

Andreoli, M. A., Hart, R. J., Ashwal, L. D., & Coetzee, H. (2006). Correlations between U, Th content and metamorphic grade in the western Namaqualand Belt, South Africa, with implications for radioactive heating of the crust. *Journal of Petrology*, *47*(6), 1095–1118. https://doi.org/10.1093/petrology/egl004

Baker, A. (1990). Stable isotopic evidence for fluid-rock interactions in the Ivrea Zone, Italy. *Journal of Petrology*, *31*(1), 243–260. https://doi.org/10.1093/petrology/31.1.243

Barboza, S. A., & Bergantz, G. W. (2000). Metamorphism and anatexis in the mafic complex contact aureole, Ivrea zone, northern Italy. *Journal of Petrology*, *41*(8), 1307–1327. https://doi.org/10.1093/petrology/41.8.1307

Barboza, S. A., Bergantz, G. W., & Brown, M. (1999). Regional granulite facies metamorphism in the Ivrea zone: Is the mafic complex the smoking gun or a red herring? *Geology*, *27*(5), 447–450. https://doi.org/10.1130/0091-7613(1999)027<0447:RGFMIT>2.3.CO;2

Bartoli, O. (2017). Phase equilibria modelling of residual migmatites and granulites: An evaluation of the melt-reintegration approach. *Journal of Metamorphic Geology*, *35*(8), 919–942. https://doi.org/10.1111/jmg.12261

Bea, F., 2012. The sources of energy for crustal melting and the geochemistry of heat-producing elements. *Lithos*, *153*, 278–291. https://doi.org/10.1016/j.lithos.2012.01.017

Bea, F. & Montero, P., 1999. Behavior of accessory phases and redistribution of Zr, REE, Y, Th, and U during metamorphism and partial melting of metapelites in the lower crust: An example from the Kinzigite Formation of Ivrea-Verbano, NW Italy. *Geochimica et Cosmochimica Acta*, *63*(7–8), 1133–1153. https://doi.org/10.1016/S0016-7037(98)00292-0

Bertolani, M. (1968). La petrografia della Valle Strona (Alpi occidentali Italiane). *Schweizerische Mineralogische Und Petrographische Mitteilungen*, *48*(3), 695–732.

Bingen, B., Demaiffe, D., & Hertogen, J. (1996). Redistribution of rare earth elements, thorium, and uranium over accessory minerals in the course of amphibolite to granulite facies metamorphism: The role of apatite and monazite in orthogneisses from southwestern Norway. *Geochimica et Cosmochimica Acta*, *60*(8), 1341–1354. https://doi.org/10.1016/0016-7037(96)00006-3

Brodie, K., & Rutter, E. (1987). Deep crustal extensional faulting in the Ivrea Zone of northern Italy. *Tectonophysics*, *140*(2–4), 193–212. https://doi.org/10.1016/0040-1951(87)90229-0

Cabella, R., Lucchetti, G., & Marescotti, P. (2001). Authigenic monazite and xenotime from pelitic metacherts in pumpellyite–actinolite-facies conditions, Sestri–Voltaggio Zone, central Liguria, Italy. *The Canadian Mineralogist*, *39*(3), 717–727. https://doi.org/10.2113/gscanmin.39.3.717

Chew, D., Petrus, J., & Kamber, B. (2014). U–Pb LA–ICPMS dating using accessory mineral standards with variable common Pb. *Chemical Geology*, *363*, 185–199. https://doi.org/10.1016/j.chemgeo.2013.11.006

Clark, C., Fitzsimons, I. C., Healy, D., & Harley, S. L. (2011). How does the continental crust get really hot? *Elements*, *7*(4), 235–240. https://doi.org/10.2113/gselements.7.4.235

Corrie, S. L., & Kohn, M. J. (2008). Trace-element distributions in silicates during prograde metamorphic reactions: Implications for monazite formation. *Journal of Metamorphic Geology*, *26*(4), 451–464. https://doi.org/10.1111/j.1525-1314.2008.00769.x

Dumond, G., Goncalves, P., Williams, M., & Jercinovic, M. (2015). Monazite as a monitor of melting, garnet growth and feldspar recrystallization in continental lower crust. *Journal of Metamorphic Geology*, *33*(7), 735–762. https://doi.org/10.1111/jmg.12150

Engi, M. (2017). Petrochronology based on REE-minerals: Monazite, allanite, xenotime, apatite. *Reviews in Mineralogy and Geochemistry*, *83*(1), 365–418. https://doi.org/10.2138/rmg.2017.83.12

Ewing, T. A., Hermann, J., & Rubatto, D. (2013). The robustness of the Zr-in-rutile and Ti-in-zircon thermometers during high-temperature metamorphism (Ivrea-Verbano zone, northern Italy). *Contributions to Mineralogy and Petrology*, *165*(4), 757–779. https://doi.org/10.1007/s00410-012-0834-5

Ewing, T. A., Rubatto, D., & Hermann, J. (2014). Hafnium isotopes and Zr/Hf of rutile and zircon from lower crustal metapelites (Ivrea–Verbano zone, Italy): Implications for chemical differentiation of the crust. *Earth and Planetary Science Letters*, *389*, 106–118. https://doi.org/10.1016/j.epsl.2013.12.029

Ewing, T. A., Rubatto, D., Beltrando, M., & Hermann, J. (2015). Constraints on the thermal evolution of the Adriatic margin during Jurassic continental break-up: U–Pb dating of rutile from the Ivrea–Verbano Zone, Italy. *Contributions to Mineralogy and Petrology*, *169*(4), 44. https://doi.org/10.1007/s00410-015-1135-6

Förster, H.-J., & Harlov, D. (1999). Monazite-(Ce)–huttonite solid solutions in granulite-facies metabasites from the Ivrea-Verbano Zone, Italy. *Mineralogical Magazine*, *63*(4), 587–594. https://doi.org/10.1180/minmag.1999.063.4.11

Foster, G., Gibson, H., Parrish, R., Horstwood, M., Fraser, J., & Tindle, A. (2002). Textural, chemical and isotopic insights into the nature and behaviour of metamorphic monazite. *Chemical Geology*, *191*(1-3), 183–207. https://doi.org/10.1016/S0009-2541(02)00156-0

Fountain, D. M. (1976). The Ivrea—Verbano and Strona-Ceneri Zones, Northern Italy: A cross-section of the continental crust—New evidence from seismic velocities of rock samples. *Tectonophysics*, *33*(1), 145–165. https://doi.org/10.1016/0040-1951(76)90054-8

Franz, G., Andrehs, G., & Rhede, D. (1996). Crystal chemistry of monazite and xenotime from Saxothuringian-Moldanubian metapelites, NE Bavaria, Germany. *European Journal of Mineralogy*, *8*(5), 1097–1118. https://doi.org/10.1127/ejm/8/5/1097

Gasser, D., Jeřábek, P., Faber, C., Stünitz, H., Menegon, L., Corfu, F., Erambert, M., & Whitehouse, M. J. (2015). Behaviour of geochronometers and timing of metamorphic reactions during deformation at lower crustal conditions: phase equilibrium modelling and U–Pb dating of zircon, monazite, rutile and titanite from the Kalak Nappe Complex, northern Norway. *Journal of Metamorphic Geology*, *33*(5), 513–534. https://doi.org/10.1111/jmg.12131

Gu, Y. (2003). Automated scanning electron microscope based mineral liberation analysis. *Journal of Minerals & Materials Characterization & Engineering*, *2*(1), 33–41. https://doi.org/10.4236/jmmce.2003.21003

Guergouz, C., Martin, L., Vanderhaeghe, O., Thébaud, N. & Fiorentini, M. (2018). Zircon and monazite petrochronologic record of prolonged amphibolite to granulite facies metamorphism in the Ivrea-Verbano and Strona-Ceneri Zones, NW Italy. *Lithos*, *308-309*, 1–18. https://doi.org/10.1016/j.lithos.2018.02.014

Hacker, B. R., Kelemen, P. B., & Behn, M. D. (2011). Differentiation of the continental crust by relamination. *Earth and Planetary Science Letters*, *307*(3), 501–516. https://doi.org/10.1016/j.epsl.2011.05.024

Hacker, B., Kylander-Clarke, A., & Holder, R. (2019). REE partitioning between monazite and garnet: Implications for petrochronology. *Journal of Metamorphic Geology*, *37*, 227–237. https://doi.org/10.1111/jmg.12458

Handy, M., Franz, L., Heller, F., Janott, B., & Zurbriggen, R. (1999). Multistage accretion and exhumation of the continental crust (Ivrea crustal section, Italy and Switzerland). *Tectonics*, *18*(6), 1154–1177. https://doi.org/10.1029/1999TC900034

Heinrich, W., Rehs, G., & Franz, G. (1997). Monazite–xenotime miscibility gap thermometry. I. an empirical calibration. *Journal of Metamorphic Geology*, *15*, 3–16. https://doi.org/10.1111/j.1525-1314.1997.t01-1-00052.x

Henk, A., Franz, L., Teufel, S., & Oncken, O. (1997). Magmatic Underplating, extension, and crustal Reequilibration: Insights from a cross-section through the Ivrea zone and Strona-Ceneri zone, Northern Italy. *The Journal of Geology*, *105*(3), 367–378. https://doi.org/10.1086/515932

Holder, R. M., Hacker, B. R., Horton, F., & Rakotondrazafy, A. M. (2018). Ultrahigh-temperature osumilite gneisses in southern Madagascar record combined heat advection and high rates of radiogenic heat production in a long-lived high-T orogen. *Journal of Metamorphic Geology*, *36*(7), 855–880. https://doi.org/10.1111/jmg.12316

Horton, F., Hacker, B., Kylander-Clark, A., Holder, R., & Jöns, N. (2016). Focused radiogenic heating of middle crust caused ultrahigh temperatures in southern Madagascar. *Tectonics*, *35*(2), 293–314. https://doi.org/10.1002/2015TC004040

Jamieson, R. A., Beaumont, C., Fullsack, P., & Lee, B. (1998). Barrovian regional metamorphism: Where's the heat? *Geological Society, London, Special Publications*, *138*(1), 23–51. https://doi.org/10.1144/GSL.SP.1996.138.01.03

Janots, E., Negro, F., Brunet, F., Goffé, B., Engi, M. & Bouybaouène, M. L. (2006). Evolution of the REE mineralogy in HP–LT metapelites of the Sebtide complex, Rif, Morocco: Monazite stability and geochronology. *Lithos*, *87*(3), 214–234. https://doi.org/10.1016/j.lithos.2005.06.008

Johnson, T. E., Clark, C., Taylor, R. J. M., Santosh, M. & Collins, A. S. (2015). Prograde and retrograde growth of monazite in migmatites: An example from the Nagercoil Block, southern India. *Geoscience Frontiers*, *6*(3), 373–387. https://doi.org/10.1016/j.gsf.2014.12.003

Karakas, O., Wotzlaw, J.-F., Guillong, M., Ulmer, P., Brack, P., Economos, R., Bergantz, G. W., Sinigoi, S., & Bachmann, O. (2019). The pace of crustal-scale magma accretion and

differentiation beneath silicic caldera volcanoes. *Geology*, *47*, 719–723. https://doi.org/10.1130/G46020.1

Kelly, N. M., Harley, S. L., & Möller, A. (2012). Complexity in the behavior and recrystallization of monazite during high-T metamorphism and fluid infiltration. *Chemical Geology*, *322*, 192–208. https://doi.org/10.1016/j.chemgeo.2012.07.001

Kelsey, D. E. & Hand, M. (2015). On ultrahigh temperature crustal metamorphism: Phase equilibria, trace element thermometry, bulk composition, heat sources, timescales and tectonic settings. *Geoscience Frontiers*, *6*(3), 311–356. https://doi.org/10.1016/j.gsf.2014.09.006

Kelsey, D. E., Clark, C., & Hand, M. (2008). Thermobarometric modelling of zircon and monazite growth in melt-bearing systems: Examples using model metapelitic and metapsammitic granulites. *Journal of Metamorphic Geology*, *26*(2), 199–212. https://doi.org/10.1111/j.1525-1314.2007.00757.x

Kirkland, C., Erickson, T., Johnson, T., Danišík, M., Evans, N., Bourdet, J., & McDonald, B. (2016). Discriminating prolonged, episodic or disturbed monazite age spectra: An example from the Kalak Nappe Complex, Arctic Norway. *Chemical Geology*, *424*, 96–110. https://doi.org/10.1016/j.chemgeo.2016.01.009

Klötzli, U. S., Sinigoi, S., Quick, J. E., Demarchi, G., Tassinari, C. C., Sato, K., & Günes, Z. (2014). Duration of igneous activity in the Sesia Magmatic System and implications for high-temperature metamorphism in the Ivrea–Verbano deep crust. *Lithos*, *206*, 19–33. https://doi.org/10.1016/j.lithos.2014.07.020

Kohn, M. J., & Malloy, M. A. (2004). Formation of monazite via prograde metamorphic reactions among common silicates: Implications for age determinations. *Geochimica et Cosmochimica Acta*, *68*(1), 101–113. https://doi.org/10.1016/S0016-7037(03)00258-8

Kretz, R. (1983). Symbols for rock-forming minerals. *American Mineralogist*, *68*(1–2), 277–279.

Kunz, B. E., & White, R. W. (2019). Phase equilibrium modelling of the amphibolite to granulite facies transition in metabasic rocks (Ivrea Zone, NW Italy). *Journal of Metamorphic Geology.*, *37*, 935–950. https://doi.org/10.1111/jmg.12478

Kunz, B. E., Johnson, T. E., White, R. W., & Redler, C. (2014). Partial melting of metabasic rocks in Val Strona di Omegna, Ivrea Zone, northern Italy. *Lithos*, *190*, 1–12. https://doi.org/10.1016/j.lithos.2013.11.015

Kunz, B. E., Regis, D., & Engi, M. (2018). Zircon ages in granulite facies rocks: Decoupling from geochemistry above 850°C? *Contributions to Mineralogy and Petrology*, *173*(3), 26. https://doi.org/10.1007/s00410-018-1454-5

Mazeina, L., Ushakov, S. V., Navrotsky, A., & Boatner, L. A. (2005). Formation enthalpy of ThSiO4 and enthalpy of the thorite→huttonite phase transition. *Geochimica et Cosmochimica Acta*, *69*(19), 4675–4683. https://doi.org/10.1016/j.gca.2005.03.053

Nemchin, A. A., Giannini, L. M., Bodorkos, S., & Oliver, N. H. S. (2001). Ostwald ripening as a possible mechanism for zircon overgrowth formation during anatexis: Theoretical constraints, a numerical model, and its application to pelitic migmatites of the Tickalara Metamorphics, northwestern Australia. *Geochimica et Cosmochimica Acta*, *65*(16), 2771–2788. https://doi.org/10.1016/S0016-7037(01)00622-6

Palya, A. P., Buick, I. S. & Bebout, G. E. (2011). Storage and mobility of nitrogen in the continental crust: Evidence from partially melted metasedimentary rocks, Mt. Stafford, Australia. *Chemical Geology*, *281*(3), 211–226. https://doi.org/10.1016/j.chemgeo.2010.12.009

Pape, J., Mezger, K., & Robyr, M. (2016). A systematic evaluation of the Zr-in-rutile thermometer in ultra-high temperature (UHT) rocks. *Contributions to Mineralogy and Petrology*, *171*(5), 44. https://doi.org/10.1007/s00410-016-1254-8

Parrish, R. R. (1990). U-Pb dating of monazite and its application to geological problems. *Canadian Journal of Earth Sciences*, *27*(11), 1431–1450. https://doi.org/10.1139/e90-152

Paton, C., Hellstrom, J., Paul, B., Woodhead, J., & Hergt, J. (2011). Iolite: Freeware for the visualisation and processing of mass spectrometric data. *Journal of Analytical Atomic Spectrometry*, *26*(12), 2508–2518. https://doi.org/10.1039/c1ja10172b

Peressini, G., Quick, J., Sinigoi, S., Hofmann, A. W., & Fanning, M. (2007). Duration of a large mafic intrusion and heat transfer in the lower crust: A SHRIMP U–Pb zircon study in the Ivrea–Verbano Zone (Western Alps, Italy). *Journal of Petrology*, *48*(6), 1185–1218. https://doi.org/10.1093/petrology/egm014

Pyle, J. M., & Spear, F. S. (1999). Yttrium zoning in garnet: Coupling of major and accessory phases during metamorphic reactions. *Geological Materials Research*, *1*(6), 1–49.

Pyle, J. M., & Spear, F. S. (2003). Four generations of accessory-phase growth in low-pressure migmatites from SW New Hampshire. *American Mineralogist*, *88*(2–3), 338–351. https://doi.org/10.2138/am-2003-2-311

Pyle, J. M., Spear, F. S., Rudnick, R. L., & McDonough, W. F. (2001). Monazite–xenotime–garnet equilibrium in metapelites and a new monazite–garnet thermometer. *Journal of Petrology*, *42*(11), 2083–2107. https://doi.org/10.1093/petrology/42.11.2083

Quick, J. E., Sinigoi, S., Snoke, A. W., Kalakay, T. J., Mayer, A. & Peressini, G., 2003. Geologic map of the southern Ivrea-Verbano Zone, northwestern Italy. US Geological Survey.

Rapp, R. P., & Watson, E. B. (1986). Monazite solubility and dissolution kinetics: Implications for the thorium and light rare earth chemistry of felsic magmas. *Contributions to Mineralogy and Petrology*, *94*(3), 304–316. https://doi.org/10.1007/BF00371439

Rapp, R. P., Ryerson, F., & Miller, C. F. (1987). Experimental evidence bearing on the stability of monazite during crustal anatexis. *Geophysical Research Letters*, *14*(3), 307–310. https://doi.org/10.1029/GL014i003p00307

Rasmussen, B., & Muhling, J. R. (2007). Monazite begets monazite: Evidence for dissolution of detrital monazite and reprecipitation of syntectonic monazite during low-grade regional metamorphism. *Contributions to Mineralogy and Petrology*, *154*(6), 675–689. https://doi.org/10.1007/s00410-007-0216-6

Redler, C., Johnson, T., White, R. W., & Kunz, B. (2012). Phase equilibrium constraints on a deep crustal metamorphic field gradient: Metapelitic rocks from the Ivrea Zone (NW Italy). *Journal of Metamorphic Geology*, *30*(3), 235–254. https://doi.org/10.1111/j.1525-1314.2011.00965.x

Redler, C., White, R. W., & Johnson, T. E. (2013). Migmatites in the Ivrea zone (NW Italy): Constraints on partial melting and melt loss in metasedimentary rocks from Val Strona di Omegna. *Lithos*, *175*, 40–53. https://doi.org/10.1016/j.lithos.2013.04.019

Rivalenti, G., Garuti, G., Rossi, A., Siena, F., & Sinigoi, S. (1981). Existence of different peridotite types and of a layered igneous complex in the Ivrea zone of the Western Alps. *Journal of Petrology*, *22*(1), 127–153. https://doi.org/10.1093/petrology/22.1.127

Robie, R. & Hemingway, B., 1995. Thermodynamic properties of minerals and related substances at 298.15 K and 1 bar (10^5 Pascals) Pressure and at higher temperatures. US Government Printing Office.

Rubatto, D., Williams, I. S., & Buick, I. S. (2001). Zircon and monazite response to prograde metamorphism in the Reynolds range, Central Australia. *Contributions to Mineralogy and Petrology*, *140*(4), 458–468. https://doi.org/10.1007/PL00007673

Rubatto, D., Hermann, J., & Buick, I. S. (2006). Temperature and bulk composition control on the growth of monazite and zircon during low-pressure anatexis (Mount Stafford, Central Australia). *Journal of Petrology*, *47*(10), 1973–1996. https://doi.org/10.1093/petrology/egl033

Rudnick, R. L., & Fountain, D. M. (1995). Nature and composition of the continental crust: A lower crustal perspective. *Reviews of Geophysics*, *33*(3), 267–309. https://doi.org/10.1029/95RG01302

Rudnick, R., & Gao, S. (2003). Composition of the continental crust. *The Crust*, Treatise on Geochemistry, (Vol. 3, pp. 1–64). Elsevier. https://doi.org/10.1016/B0-08-043751-6/03016-4

Rutter, E., Brodie, K., James, T., & Burlini, L. (2007). Large-scale folding in the upper part of the Ivrea-Verbano zone, NW Italy. *Journal of Structural Geology*, *29*(1), 1–17. https://doi.org/10.1016/j.jsg.2006.08.013

Schmid, R., & Wood, B. J. (1976). Phase relationships in granulitic metapelites from the Ivrea-Verbano zone (northern Italy). *Contributions to Mineralogy and Petrology*, *54*(4), 255–279. https://doi.org/10.1007/bf00389407

Schnetger, B. (1994). Partial melting during the evolution of the amphibolite-to granulite-facies gneisses of the Ivrea zone, northern Italy. *Chemical Geology*, *113*(1–2), 71–101. https://doi.org/10.1016/0009-2541(94)90006-X

Schulz, B. (2017). Polymetamorphism in garnet micaschists of the Saualpe Eclogite unit (eastern Alps, Austria), resolved by automated SEM methods and EMP–Th–U–Pb monazite dating. *Journal of Metamorphic Geology*, *35*(2), 141–163. https://doi.org/10.1111/jmg.12224

Shaw, D. M. (1956). Geochemistry of pelitic rocks. Part III: Major elements and general geochemistry. *Geological Society of America Bulletin*, *67*(7), 919–934. https://doi.org/10.1130/0016-7606(1956)67[919:GOPRPI]2.0.CO;2

Sills, J. D., & Tarney, J. (1984). Petrogenesis and tectonic significance of amphibolites interlayered with metasedimentary gneisses in the Ivrea Zone, Southern Alps, Northwest Italy. *Tectonophysics*, *107*(3–4), 187–206. https://doi.org/10.1016/0040-1951(84)90251-8

Sinigoi, S., Quick, J. E., Clemens-Knott, D., Mayer, A., Demarchi, G., Mazzucchelli, M., Negrini, L., & Rivalenti, G. (1994). Chemical evolution of a large mafic intrusion in the lower crust, Ivrea-Verbano zone, northern Italy. *Journal of Geophysical Research: Solid Earth*, *99*(B11), 21575–21590. https://doi.org/10.1029/94JB00114

Skrzypek, E., Kato, T., Kawakami, T., Sakata, S., Hattori, K., Hirata, T., & Ikeda, T. (2018). Monazite behaviour and time-scale of metamorphic processes along a low-pressure/high-temperature field gradient (Ryoke belt, SW Japan). *Journal of Petrology*, *59*(6), 1109–1144. https://doi.org/10.1093/petrology/egy056

Smith, H. A., & Barreiro, B. (1990). Monazite U-Pb dating of staurolite grade metamorphism in pelitic schists. *Contributions to Mineralogy and Petrology*, *105*(5), 602–615. https://doi.org/10.1007/BF00302498

Spear, F. S. (2010). Monazite–allanite phase relations in metapelites. *Chemical Geology*, *279*(1–2), 55–62. https://doi.org/10.1016/j.chemgeo.2010.10.004

Spear, F. S., & Pyle, J. M. (2010). Theoretical modeling of monazite growth in a low-Ca metapelite. *Chemical Geology*, *273*(1), 111–119. https://doi.org/10.1016/j.chemgeo.2010.02.016

Spencer, C. J., Kirkland, C. L., & Taylor, R. J. (2016). Strategies towards statistically robust interpretations of in situ U–Pb zircon geochronology. *Geoscience Frontiers*, *7*(4), 581–589. https://doi.org/10.1016/j.gsf.2015.11.006

Stepanov, A. S., Hermann, J., Rubatto, D., & Rapp, R. P. (2012). Experimental study of monazite/melt partitioning with implications for the REE, Th and U geochemistry of crustal rocks. *Chemical Geology*, *300*, 200–220. https://doi.org/10.1016/j.chemgeo.2012.01.007

Stepanov, A. S., Hermann, J., Korsakov, A. V., & Rubatto, D. (2014). Geochemistry of ultrahigh-pressure anatexis: Fractionation of elements in the Kokchetav gneisses during melting at diamond-facies conditions. *Contributions to Mineralogy and Petrology*, *167*(5), 1002. https://doi.org/10.1007/s00410-014-1002-x

Taylor, R. J. M., Clark, C., Fitzsimons, I. C., Santosh, M., Hand, M., Evans, N., & McDonald, B. (2014). Post-peak, fluid-mediated modification of granulite facies zircon and monazite in the Trivandrum Block, southern India. *Contributions to Mineralogy and Petrology*, *168*(2), 1044. https://doi.org/10.1007/s00410-014-1044-0

Taylor, R. J. M., Kirkland, C. L. & Clark, C. (2016). Accessories after the facts: Constraining the timing, duration and conditions of high-temperature metamorphic processes. *Lithos*, *264*, 239–257. https://doi.org/10.1016/j.lithos.2016.09.004

Vavra, G., & Schaltegger, U. (1999). Post-granulite facies monazite growth and rejuvenation during Permian to lower Jurassic thermal and fluid events in the Ivrea zone (southern Alps). *Contributions to Mineralogy and Petrology*, *134*(4), 405–414. https://doi.org/10.1007/s004100050493

Vavra, G., Gebauer, D., Schmid, R., & Compston, W. (1996). Multiple zircon growth and recrystallization during polyphase late carboniferous to Triassic metamorphism in granulites of the Ivrea zone (southern Alps): An ion microprobe (SHRIMP) study. *Contributions to Mineralogy and Petrology*, *122*(4), 337–358. https://doi.org/10.1007/s004100050132

Vavra, G., Schmid, R., & Gebauer, D. (1999). Internal morphology, habit and U-Th-Pb microanalysis of amphibolite-to-granulite facies zircons: Geochronology of the Ivrea zone (southern Alps). *Contributions to Mineralogy and Petrology*, *134*(4), 380–404. https://doi.org/10.1007/s004100050492

Watt, G. R. (1995). *High-thorium monazite-(Ce) formed during disequilibrium melting of metapelites under granulite-facies*

conditions (Vol. 59) (pp. 735–743). De Gruyter. https://doi.org/10.1180/minmag.1995.059.397.14

Wawrzenitz, N., Krohe, A., Rhede, D., & Romer, R. L. (2012). Dating rock deformation with monazite: The impact of dissolution precipitation creep. *Lithos*, *134*, 52–74. https://doi.org/10.1016/j.lithos.2011.11.025

Williams, I. (2001). Response of detrital zircon and monazite, and their U–Pb isotopic systems, to regional metamorphism and host-rock partial melting, Cooma Complex, southeastern Australia. *Australian Journal of Earth Sciences*, *48*(4), 557–580. https://doi.org/10.1046/j.1440-0952.2001.00883.x

Williams, M. A., 2019. Thorium substitution in monazite: Case studies and forward modelling. University of Adelaide (Doctoral dissertation). https://hdl.handle.net/2440/130727

Williams, M. A., Kelsey, D. E., Baggs, T., Hand, M. & Alessio, K. L., 2018. Thorium distribution in the crust: Outcrop and grain-scale perspectives. *Lithos*, *320-321*, 222–235. https://doi.org/10.1016/j.lithos.2018.09.016

Wing, B. A., Ferry, J. M., & Harrison, T. M. (2003). Prograde destruction and formation of monazite and allanite during contact and regional metamorphism of pelites: Petrology and geochronology. *Contributions to Mineralogy and Petrology*, *145*(2), 228–250. https://doi.org/10.1007/s00410-003-0446-1

Wolff, R., Dunkl, I., Kiesselbach, G., Wemmer, K., & Siegesmund, S. (2012). Thermochronological constraints on the multiphase exhumation history of the Ivrea-Verbano zone of the southern Alps. *Tectonophysics*, *579*, 104–117. https://doi.org/10.1016/j.tecto.2012.03.019

Yakymchuk, C. (2017). Behaviour of apatite during partial melting of metapelites and consequences for prograde suprasolidus monazite growth. *Lithos*, *274*, 412–426. https://doi.org/10.1016/j.lithos.2017.01.009

Yakymchuk, C., & Brown, M. (2014). Behaviour of zircon and monazite during crustal melting. *Journal of the Geological Society*, *171*(4), 465–479. https://doi.org/10.1144/jgs2013-115

Yakymchuk, C., & Brown, M. (2019). Divergent behaviour of Th and U during anatexis: Implications for the thermal evolution of orogenic crust. *Journal of Metamorphic Geology*, *37*, 899–916. https://doi.org/10.1111/jmg.12469

Yakymchuk, C., Kirkland, C. L., & Clark, C. (2018). Th/U ratios in metamorphic zircon. *Journal of Metamorphic Geology*, *36*(6), 715–737. https://doi.org/10.1111/jmg.12307

Yang, P., & Pattison, D. (2006). Genesis of monazite and Y zoning in garnet from the Black Hills, South Dakota. *Lithos*, *88*(1–4), 233–253. https://doi.org/10.1016/j.lithos.2005.08.012

Zingg, A., Handy, M., Hunziker, J. & Schmid, S. (1990). Tectonometamorphic history of the Ivrea zone and its relationship to the crustal evolution of the southern Alps. *Tectonophysics*, *182*(1–2), 169–192, 192. https://doi.org/10.1016/0040-1951(90)90349-D

SUPPORTING INFORMATION

Additional supporting information may be found in the online version of the article at the publisher's website.

Table S1. Whole rock geochemistry for Ivrea-Verbano metapelite samples.

Appendix S2. Detailed analytical technique for LA–ICP–MS monazite geochronology and trace element analysis.

Table S2.1. Measured isotopes and dwell times for LA–ICP–MS analysis.

Figure S2.1. Wetherill and Tera–Wasserburg plots of uncorrected monazite U–Pb geochronology with data arranged by sample. Bold black line is the regression line for the initial $^{207}Pb/^{206}Pb$ ratio ($^{207}Pb/^{206}Pb_0$) used in the 207 Pb correction, $^{207}Pb/^{206}Pb_0 = 0.805976$.

Figure S2.2. Tera–Wasserburg plot of uncorrected monazite U–Pb geochronology with data arranged by monazite zone (Z1–Z9). Zones are described in main text. Bold black line is the regression line for the initial $^{207}Pb/^{206}Pb$ ratio ($^{207}Pb/^{206}Pb_0$) used in the 207 Pb correction, $^{207}Pb/^{206}Pb_0 = 0.805976$.

Table S3. Uncorrected LA–ICP–MS monazite geochronology data.

Appendix S4. Detailed accessory mineral petrography.

Figure S4.1. Electron microprobe element maps showing retrograde reactions affecting monazite in IV16–16. Aln, allanite–Th-orthosilicate aggregates; ap, apatite–cheralite aggregates; mnz, monazite.

How to cite this article: Williams, M. A., Kelsey, D. E., & Rubatto, D. (2022). Thorium zoning in monazite: A case study from the Ivrea–Verbano zone, NW Italy. *Journal of Metamorphic Geology*, 1–28. https://doi.org/10.1111/jmg.12656